



Article

# Small Scale Landslide Detection Using Sentinel-1 Interferometric SAR Coherence

Marios Tzouvaras <sup>1,2,\*</sup> , Chris Danezis <sup>1,2</sup>  and Diofantos G. Hadjimitsis <sup>1,2</sup>

<sup>1</sup> Department of Civil Engineering and Geomatics, Cyprus University of Technology, Limassol 3036, Cyprus; chris.danezis@cut.ac.cy (C.D.); d.hadjimitsis@cut.ac.cy (D.G.H.)

<sup>2</sup> ERATOSTHENES Centre of Excellence, Limassol 3036, Cyprus

\* Correspondence: marios.tzouvaras@cut.ac.cy

Received: 7 April 2020; Accepted: 12 May 2020; Published: 15 May 2020



**Abstract:** Infrastructure is operational under normal circumstances and is designed to cope with common natural disruptions such as rainfall and snow. Natural hazards can lead to severe problems at the areas where such phenomena occur, but also at neighboring regions as they can make parts of a road network virtually impassable. Landslides are one of the most devastating natural hazards worldwide, triggered by various factors that can be monitored via ground-based and/or satellite-based techniques. Cyprus is in an area of high susceptibility to such phenomena. Currently, extensive field campaigns including geotechnical drilling investigations and geophysical excavations are conducted to monitor land movements, and, at the same time, determine the geological suitability of areas. Active satellite remote sensors, namely Synthetic Aperture Radar (SAR), have been widely used for detecting and monitoring landslides and other ground deformation phenomena using Earth Observation based techniques. This paper aims to demonstrate how the use of Copernicus open-access and freely distributed datasets along with the exploitation of the open-source processing software SNAP (Sentinel's Application Platform), provided by the European Space Agency, can be used for landslide detection, as in the case study near Pissouri, where a landslide was triggered by heavy rainfall on 15 February 2019, which caused a major disturbance to everyday commuters since the motorway connecting the cities of Limassol and Paphos remained closed for more than a month. The Coherent Change Detection (CCD) methodology was applied successfully by detecting the phenomenon under study accurately, using two indicators (the coherence difference and the normalized coherence difference). Receiver Operating Characteristic (ROC) analysis was carried out to measure their performance with the coherence difference having an overall accuracy of 93% and the normalized coherence difference having an overall accuracy of 94.8% for detecting the landslide and non-landslide areas. The probability of landslide detection was 63.2% in the case of the coherence difference and increased to 73.7% for the normalized coherence difference, whereas the probability of false alarm for both indicators was approximately 1%.

**Keywords:** coherence; change detection; landslides; rainfall; CCD; SAR; Copernicus; Sentinel-1; early warning systems

## 1. Introduction

Infrastructure is designed to be operational under normal circumstances and to cope with common natural disruptions such as rainfall, snow, and excessive heat. However, natural hazards can lead to severe problems not only at the areas where such events occur, but also at neighboring regions or even the entire country since they can make parts of a road network virtually impassable [1]. Given the value of a functional road transportation system, it is of great importance to be able to predict the

impacts of disruptions to the system, their most likely location, and where their impacts would be the most severe [2].

The reliability of critical civil infrastructure, such as transportation systems, is of key interest during all the stages of planning and construction, from the conception of the idea until its realization. Infrastructure users, planners, and designers at all levels, both in the public and private sectors, and many other stakeholders are involved during this process [3]. Moreover, the safety of citizens and infrastructure users is of the greatest importance. Thus, built-up areas must be properly specified, after careful and considerate planning by the relevant responsible authorities, in geologically suitable areas with low risk for various natural hazards.

In Cyprus, extreme weather conditions such as drought and heavy rainfall can lead to amplification of the soil erosion processes. Furthermore, Cyprus is in an area of high susceptibility to seismic activities and landslides. The main geotechnical problems that take place are landslides, rock falls, and ground subsidence, which pose a constant threat for built-up areas and civil infrastructure, such as roads, bridges and tunnels. Cyprus is frequently affected by catastrophic earthquakes due to its position at the tectonic boundary between the African and Eurasian lithospheric plate in the Eastern Mediterranean region, as presented in Figure 1.

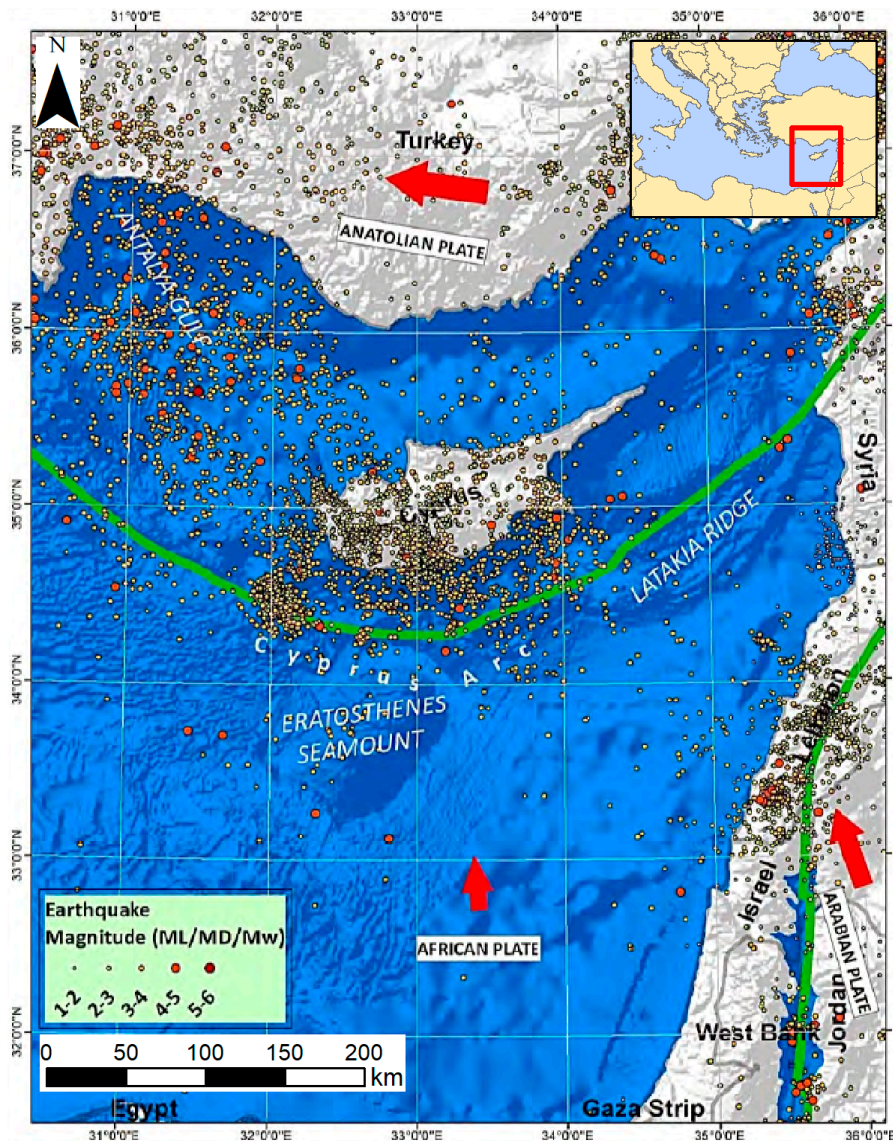


Figure 1. The Cyprus Arc and the adjacent tectonic plates [4].

In the western part of Cyprus, especially in the Paphos District, relatively large landslides take place, due to the presence of geological formations prone to landslides, like the Mamonía mélange and the Kannaviou bentonitic clays [5]. In Limassol District, located in the southwestern part of the island, landslide phenomena take place less frequently, related mainly to the Lower Marls of the Lefkara Formation as well as the Moni Formation. Rockfalls are observed mostly in the mountainous areas of Cyprus and in natural and manmade slopes. Last but not least, due to the nature of the main soil types in Cyprus ground, i.e., marls, clays, and sulfates, ground subsidence is a frequent phenomenon, as it is highly related to the geological conditions and the mechanical properties of the ground itself. Under adverse morphological and hydrogeological conditions, hazardous landslides can occur in areas even when formations prone to landslides are not present [5,6].

To date, the combined result of landslides and earthquakes in Cyprus has led to the abandonment and relocation of many villages, especially in Paphos District, and caused the destruction of properties, infrastructure, and road networks. In Cyprus, current infrastructure for monitoring and studying these natural hazards is limited to conventional equipment, such as seismographs, geophones, and inclinometers [7]. Thus, no systematic research has been conducted to monitor ground deformation with high accuracy and dense spatial resolution in a timely manner.

Several geotechnical field investigations have been conducted by the Geological Survey Department (GSD) of Cyprus in collaboration with the British Geological Survey between 1985 and 1986 in Paphos District, and especially in the villages of Agios Photios, Kannaviou, Pandalia, and Simou, which are areas prone to landslides [8,9]. Extensive research has been conducted to study several slope failures in Cyprus through extensive geological and geotechnical investigations, and interpretation of aerial photographs and QuickBird high-resolution satellite imagery for observation and verification of the results [10–13]. All studies emphasized the effect and the importance of landslide hazards, especially in the western part of Cyprus.

In Cyprus, the GSD of the Ministry of Agriculture, Natural Resources and Environment are responsible for conducting studies related to natural geological hazards such as landslides and land subsidence [7]. An inventory of all landslide events that occurred in Cyprus was developed by the GSD based on these studies, as presented in Figure 2, and is continuously updated based on new ground deformation events that take place. It is clear that the vast majority of the landslides that occurred in Cyprus took place in the Paphos District.

Furthermore, GSD are responsible for determining the geological suitability zones in Cyprus. This includes the preparation of specialized geotechnical drilling investigations, geological mapping activities, and geophysical excavations to obtain the required information for the planning and safe urban development of an area. To date, the geological suitability map (Figure 3) covers only approximately 9.65% of Cyprus, and more specifically (a) the mountainous and semi-mountainous Paphos District, and small parts of (b) Limassol, (c) Larnaca, and (d) Famagusta [7].

Optical satellite remote sensing techniques have been widely used in landslide susceptibility assessment in terms of development of landslide inventory maps [14–18]. Moreover, several studies have been carried out on investigating the effectiveness of Differential SAR Interferometry (DInSAR) for detecting land movements. DInSAR has been used successfully for monitoring land subsidence and uplift [19–24] with particular applications such as landslides [25–27] and other ground displacements caused by natural occurring phenomena such as earthquakes [28–30], volcano eruptions [31–34], and human activities [35,36]. Last but not least, DInSAR has proved to be effective in identifying damage in large civil infrastructure like roads and road networks [37], assisting in that way in the planning of infrastructure maintenance works.

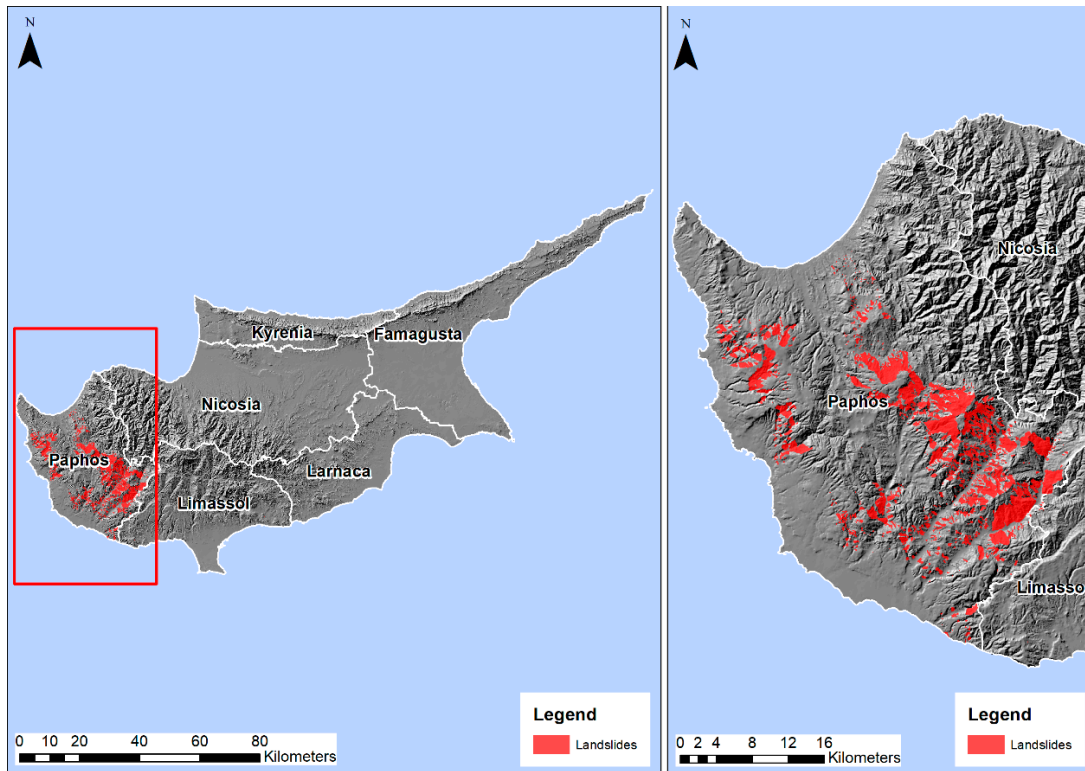


**Figure 2.** Landslide inventory map of Cyprus. Landslides occur mostly on the western part of the island. Digitized map based on data provided by the Cyprus Geological Survey Department.

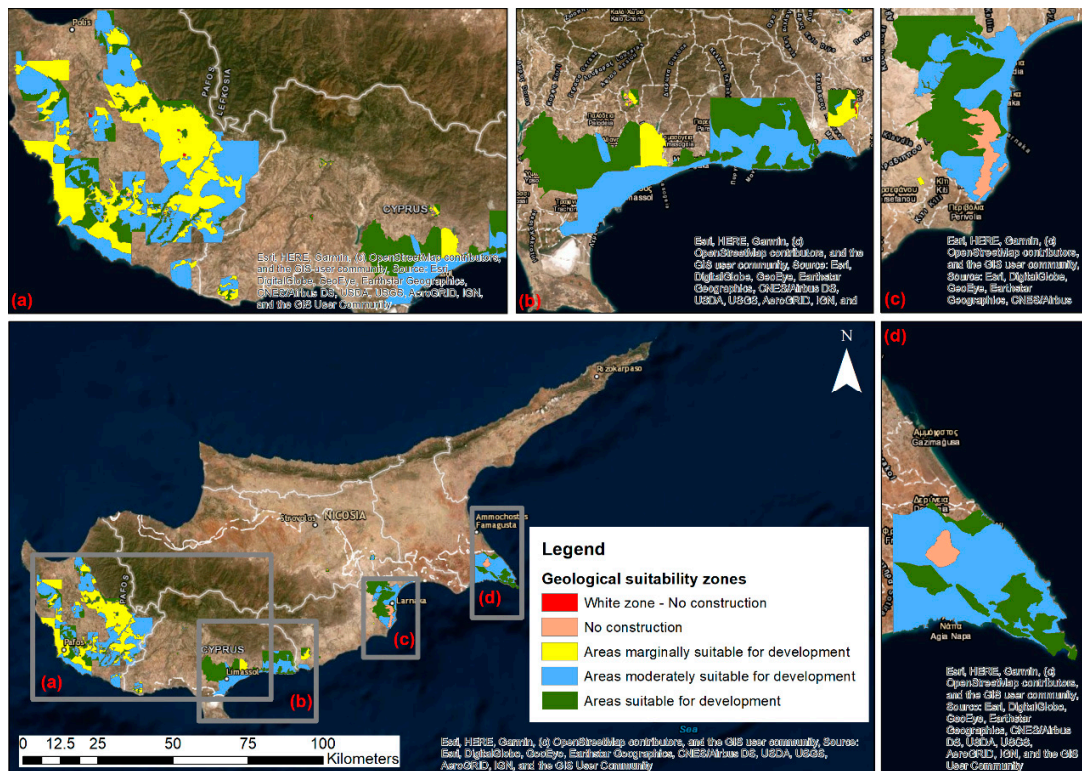


**Figure 3.** Geological suitability zone map of Cyprus. It covers (a) the mountainous and semi-mountainous Paphos District, and small parts of (b) Limassol, (c) Larnaca, and (d) Famagusta. Digitized map based on data provided by the Cyprus Geological Survey Department.

Interferometric coherence has also been used to monitor changes in topography, but being a statistical value, it cannot provide quantitative information about ground displacement [38]. Coherence is a product of the DInSAR methodology and a measure of the quality of the produced interferogram. It describes the similarity of the reflected radar signal between two images [39]. SAR coherence  $\gamma$  can be calculated by using Equation (1), where  $n$  is the number of pixels,  $A_i$  and  $B_i$  are the SAR images  $A$  (master) and  $B$  (slave), respectively, and the  $*$  denotes the complex conjugate.

$$\gamma = \frac{\frac{1}{n} \left| \sum_{i=1}^n A_i \times B_i^* \right|}{\sqrt{\frac{1}{n} \left( \sum_{i=1}^n A_i \times A_i^* \sum_{i=1}^n B_i \times B_i^* \right)}} \quad (1)$$

It ranges from 0, i.e., complete phase decorrelation (interferometric phase is pure noise), to 1, i.e., complete phase correlation [39,40]. The overall coherence of a single pixel is determined by a number of factors and is usually expressed by Equation (2), as follows:

$$\gamma_{\text{overall}} = \gamma_{\text{thermal}} \cdot \gamma_{\text{spatial}} \cdot \gamma_{\text{temporal}} \quad (2)$$

where  $\gamma_{\text{temporal}}$  is the temporal component of coherence,  $\gamma_{\text{spatial}}$  is the spatial component of coherence, and  $\gamma_{\text{thermal}}$  is the thermal component of coherence [41]. If one or more of the three components of coherence decorrelates, the radar signal will also decorrelate. Thermal coherence is related to radar signal noise, and its decorrelation is rather insignificant [41]. Spatial coherence depends on the area's topography, and the characteristics of the satellite, such as the geometry of image acquisition and the radar wavelength [41,42].

On the other hand, the temporal component of coherence depends on changes on the ground surface, which appears as variations in the scattering properties of the target pixels in the area of interest between the two SAR images of the interferometric pair [41–43]. To detect these changes, the two images must be taken of the same scene with the same incident angle, but at different times. Any changes in the reflectivity of the scene are recorded as a phase decorrelation of the pixels between the two images [38,39]. Thus, even the smallest changes in an area of interest, between two images, can be detected, by means of a reduction in the temporal component of coherence and, consequently, in the overall coherence. In general, a random change of the position and physical properties of a specific point on the surface of the Earth can be detected as low coherence of a pair of images [39].

The Coherent Change Detection (CCD) technique has been used in several applications such as monitoring land use / land cover changes [44–48] as well as agricultural studies [49–51] and forestry applications [52–56], and, lately, in earthquake impact assessment studies [42,43,57–59]. The CCD technique is less efficient in areas with high human activity, or where the underlying geological formations are too hard to record detectable surface modifications. Seasonal variations, such as varying weather conditions, can also affect the estimated coherence [39,43,60]. Steep slopes, forests, and areas with high moisture can lead to a decorrelated phase signal in less than a day. Vegetated or water surfaces, due to their continuous variations, appear to have low coherence values [38,61]. Moreover, coherence values decrease with larger image temporal baselines and larger perpendicular baseline lengths between the two images. Co-registration must be performed accurately, as it significantly affects the coherence map [39,61–63]. Last but not least, the poor resampling can lead to low coherence during InSAR processing [38,40,41,60]. However, the identification of changes in coherence through Interferometric SAR processing can provide useful information for the rapid detection of natural hazards [59,64,65].

The main aim of the present study is to assess the performance of the Coherent Change Detection methodology to detect a landslide that was triggered by heavy rainfall on 15 February 2019, in a suburban area next to the motorway connecting the cities of Limassol and Paphos, through the exploitation of free Sentinel-1 datasets provided by the Copernicus programme and the freely available open-source software Sentinel's Application Platform (SNAP) developed by ESA. The area of study

is presented in the next section of the present study. Next, the materials and methodology used are presented in Section 3. The results from the applied methodology are presented in Section 4. Lastly, results are being discussed in Sections 5 and 6 including the concluding remarks.

## 2. Area of Study

The case study area is located in Limassol District, at the south-west part of the island, near the village of Pissouri. The area lies next to the A6 motorway connecting the cities of Limassol and Paphos, with thousands of people commuting every day using the specific part of the road network. The extents of the case study area and the specific parts of the roads that was closed due to the landslide event is shown below in Figure 4.



**Figure 4.** The case study area along the A6 motorway near Pissouri.

The geology of the area consists of rocks with various mechanical properties related to resistance to erosion and weathering, such as bentonite, lava, limestone, quartz sandstone, argillaceous shale and hornstone, serpentinite, pyroxenite, gabbro, chalks, and marls [66]. The most resistant rocks lie over the very soft and fragmented masses. The geology of the case study area as well as in areas adjacent to it is presented in Figure 5.

Pissouri, which is located at the south-east part of the case study area, is covered by sediments of Pliocene-Pleistocene age, most notably calcarenites, carbonate marls, and sandstones of the Nicosia formation, as in the case of the case study area near the A6 motorway. Underneath lies the Pissouri marl, which is characterized by sandy interlayers. The marlstone is susceptible to fast weathering. In most sites, the fresh marl is covered by a layer of weathered marl [67].

In this area, the soils are particularly problematic and prone to landslides, rockslides, and other geotechnical failures. During the last decade, numerous landslide and rockslide events have occurred in the wider region, triggered mainly by extreme rainfall, having a significant impact to citizens as they led to road closures due to the proximity of the “problematic” soils to the road network (new and old motorway) connecting the cities of Limassol and Paphos. Rehabilitation works were carried

out to remove soil, mud, and rocks from the road, caused by the landslides. Traffic was diverted to alternative routes, causing significant disruption for the everyday commute.

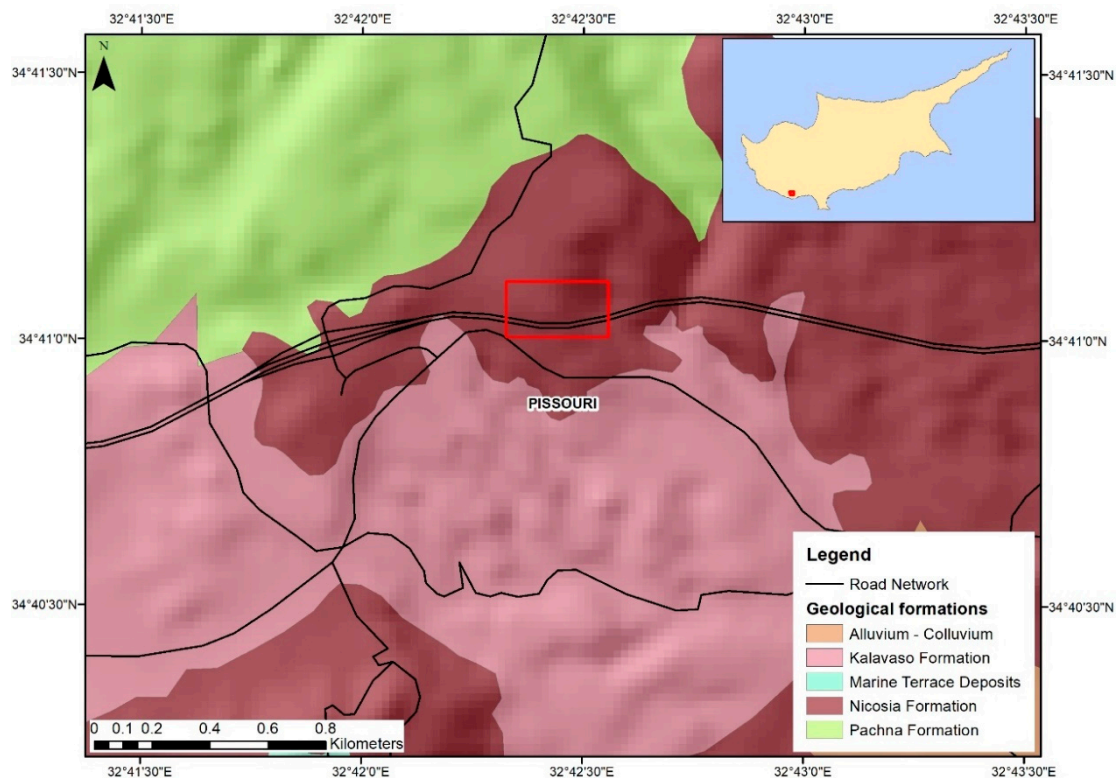


**Figure 5.** The geology of the wider area surrounding the case study near Pissouri.

The landslide event under study occurred on 15 February 2019, following substantial rainfall, next to the Paphos—Limassol motorway A6, in the direction from Paphos to Limassol between exits of Avdimou and Pissouri (Figure 6). Extensive earthworks were carried out to remove the disturbed soil and the Paphos-Limassol motorway was again open to traffic on 23 March 2019.

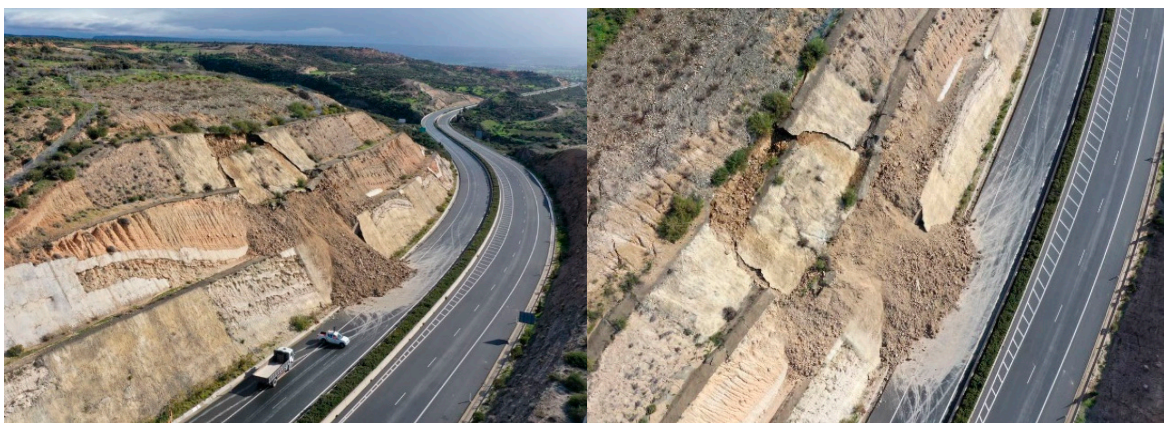


**Figure 6.** Side and top views of the landslide on the Paphos-Limassol motorway near Pissouri. Both photos were provided by the Geological Survey Department of Cyprus.

### 3. Materials and Methods

Sentinel-1 SAR acquisitions were downloaded from the European Space Agency (ESA) Copernicus Open Access Hub [68] to study the impact of the landslide to infrastructure in the case study near Pissouri, described before.

Since the landslide under study affected critical infrastructure, it is of great importance to raise awareness of an upcoming danger in a timely manner. As noted in literature, it is the first time that the CCD methodology is applied for landslides induced by heavy rainfall. Thus, its development and evolution needed to be investigated in detail. Due to the nature and complexity of the landslide under investigation, 32 Sentinel-1 Interferometric Wide (IW) swath SLC of VV + VH polarization, 16 Sentinel-1A and 16 Sentinel-1B, images were downloaded for the period of 11 January 2019–12 April 2019, to carry out a comprehensive study on the evolution of the landslide.

The processing of Sentinel-1 SAR acquisitions was carried out using the open-source software Sentinel Applications Platform (SNAP) (version 7.0, as of 22 July 2019) [69]. A total of 28 interferometric SAR pairs were formed, with all images in the respective SAR pairs being acquired 12 days apart to minimize the effects of atmosphere and topography on the results (Figure 7). The interferometric SAR pairs and their characteristics are presented below in Table 1, in ascending order based on the master image acquisition date. There was no restriction in terms of satellite pass direction since the slope that was deformed faces southwards, which allows the use of both ascending and descending SAR images.

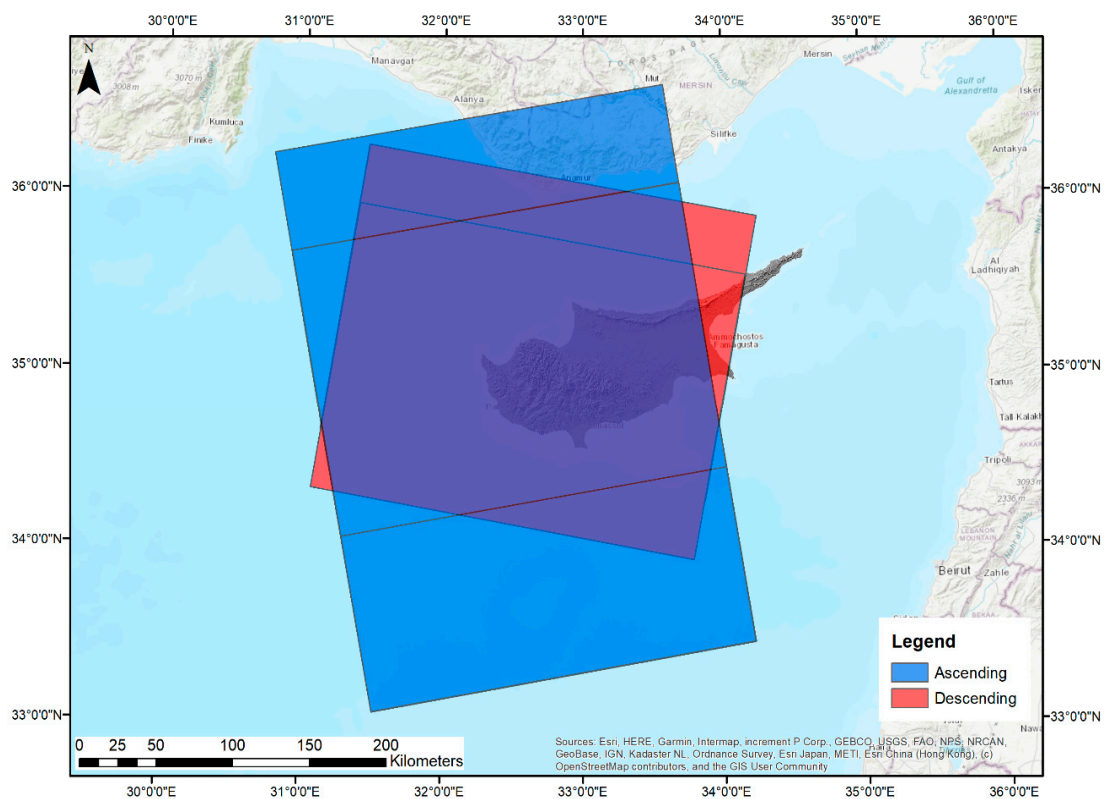


**Figure 7.** Sentinel-1 Synthetic Aperture Radar (SAR) acquisitions—11 January 2019–12 April 2019.

The suitability of all SAR image pairs was checked via an overview of the perpendicular baseline and the modelled coherence. The perpendicular baselines for all pairs were shorter than the threshold of 200 m that was set, which is very common for Sentinel-1 imagery as they favor rather small perpendicular baselines. Moreover, all pairs show high modelled coherence nearly equal to or greater than 0.90. However, the modelled coherence shown above is only an estimate. The actual coherence of the interferometric pairs was calculated after the completion of the step of the interferogram formation.

Following the selection of appropriate SAR pairs, the TOPSAR split was performed, where the sub-swath, burst, and polarization of the images comprising each SAR pair were selected. In all cases, the sub-swath IW2 and polarization VV were selected in the processing parameters whereas the number of bursts was reduced in order to reduce the processing time. On the split products developed in the previous step, Sentinel Precise Orbits, automatically downloaded from SNAP, were applied



to determine the exact position of the satellite during the acquisition of SAR data. Then, the SRTM (Shuttle Radar Topography Mission) 1 sec HGT Digital Elevation Model (DEM) with a spatial resolution of 30 m, downloaded automatically from SNAP, and the bilinear interpolation method for the DEM resampling were selected, to carry out the co-registration of the SAR image pairs. Moreover, Enhanced Spectral Diversity (ESD) was used to increase the quality of the co-registration by applying range and azimuth shift corrections to the slave image.

**Table 1.** Synthetic Aperture Radar (SAR) image interferometric pairs.

No.	Platform	Date (Master)	Date (Slave)	Pass Direction	Temp. Baseline	Perp. Baseline	Modelled Coherence
1	Sentinel-1A	11/01/2019	23/01/2019	Ascending	12 days	16.36 m	0.98
2	Sentinel-1A	12/01/2019	24/01/2019	Descending	12 days	108.39 m	0.90
3	Sentinel-1B	17/01/2019	29/01/2019	Ascending	12 days	43.40 m	0.95
4	Sentinel-1B	18/01/2019	30/01/2019	Descending	12 days	34.79 m	0.96
5	Sentinel-1A	23/01/2019	04/02/2019	Ascending	12 days	155.91 m	0.86
6	Sentinel-1A	24/01/2019	05/02/2019	Descending	12 days	79.26 m	0.92
7	Sentinel-1B	29/01/2019	10/02/2019	Ascending	12 days	23.22 m	0.97
8	Sentinel-1B	30/01/2019	11/02/2019	Descending	12 days	46.48 m	0.95
9	Sentinel-1A	04/02/2019	16/02/2019	Ascending	12 days	102.44 m	0.90
10	Sentinel-1A	05/02/2019	17/02/2019	Descending	12 days	12.46 m	0.98
11	Sentinel-1B	10/02/2019	22/02/2019	Ascending	12 days	17.44 m	0.97
12	Sentinel-1B	11/02/2019	23/02/2019	Descending	12 days	86.63 m	0.92
13	Sentinel-1A	16/02/2019	28/02/2019	Ascending	12 days	84.72 m	0.92
14	Sentinel-1A	17/02/2019	01/03/2019	Descending	12 days	14.88 m	0.97
15	Sentinel-1B	22/02/2019	06/03/2019	Ascending	12 days	63.25 m	0.94
16	Sentinel-1B	23/02/2019	07/03/2019	Descending	12 days	10.12 m	0.98
17	Sentinel-1A	28/02/2019	12/03/2019	Ascending	12 days	3.15 m	0.99
18	Sentinel-1A	01/03/2019	13/03/2019	Descending	12 days	87.86 m	0.92
19	Sentinel-1B	06/03/2019	18/03/2019	Ascending	12 days	30.08 m	0.96
20	Sentinel-1B	07/03/2019	19/03/2019	Descending	12 days	75.78 m	0.93
21	Sentinel-1A	12/03/2019	24/03/2019	Ascending	12 days	17.67 m	0.97
22	Sentinel-1A	13/03/2019	25/03/2019	Descending	12 days	63.94 m	0.93
23	Sentinel-1B	18/03/2019	30/03/2019	Ascending	12 days	82.29 m	0.92
24	Sentinel-1B	19/03/2019	31/03/2019	Descending	12 days	9.54 m	0.98
25	Sentinel-1A	24/03/2019	05/04/2019	Ascending	12 days	51.98 m	0.94
26	Sentinel-1A	25/03/2019	06/04/2019	Descending	12 days	57.14 m	0.94
27	Sentinel-1B	30/03/2019	11/04/2019	Ascending	12 days	30.86 m	0.96
28	Sentinel-1B	31/03/2019	12/04/2019	Descending	12 days	24.92 m	0.97

The co-registered SAR pair was then used to develop the coherence maps. This was achieved after subtracting the flat-earth phase using a 5<sup>th</sup> degree “Flat Earth” polynomial and 501 estimation points, and the removal of the topographic phase using an SRTM 1 sec HGT DEM. After this step, the interferograms of the SAR pairs were also created.

Then, the TOPSAR Deburst tool was used to remove the seamlines between the single bursts of the coherence products. These coherence maps were then geometrically corrected for SAR geometric distortions using a digital elevation model (DEM) and producing a map projected product. The Range-Doppler Terrain correction was used after selecting the SRTM 1 sec HGT DEM and the bilinear interpolation method for image and DEM resampling. The resulting coherence maps were projected in WGS84 with a pixel size of 11.4 m × 11.4 m.

In total, 28 coherence maps were developed following the methodology, as presented in Figure 8, based on the formed interferometric SAR image pairs. All coherence maps were then stacked together, using geolocation as the initial offset method based on the coherence map of the first interferometric pair dated 11 January 2019–23 January 2019 as the master image, to assist in the comparison of results on the same basis.

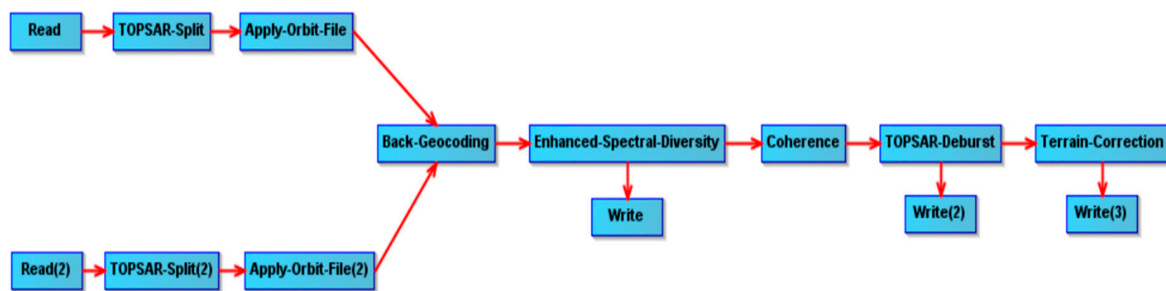


**Figure 8.** Coherence maps development methodology. The workflow was created in the Graph Builder tool in Sentinel’s Application Platform (SNAP) software.

Lastly, the geolocated coherence maps were grouped in three individual stacks, i.e., pre-event, co-event, and post-event, as shown in Figure 9, for further comparison. The results from different pass directions of Sentinel-1A and Sentinel-1B were studied individually.

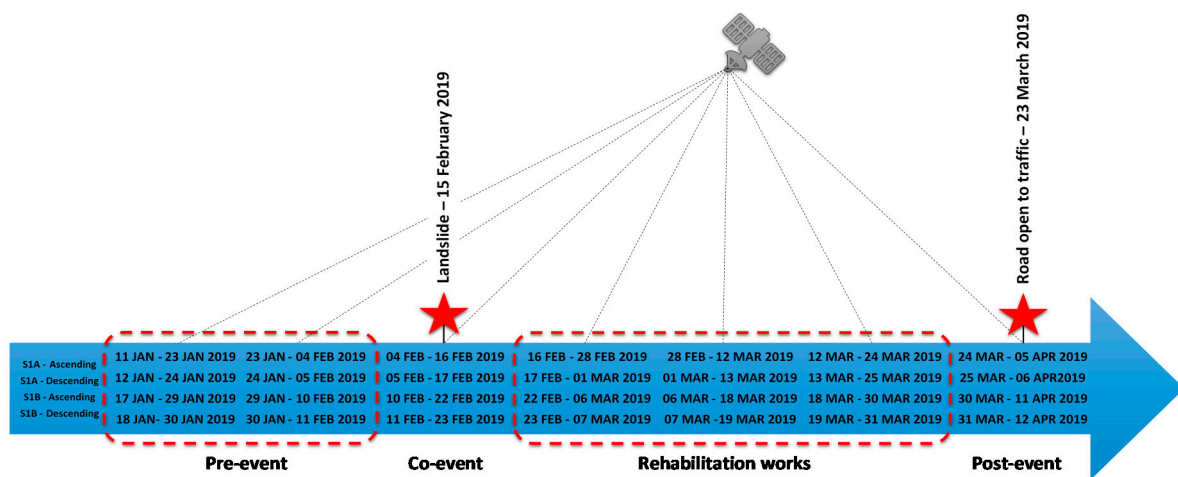


**Figure 9.** Timeline of Synthetic Aperture Radar (SAR) acquisitions and events.

All the details about the specific landslide, such as the exact landslide outline, the extents of rehabilitation works, and their duration, as well as the exact date of the road re-opening back to the traffic were known. However, as our study aims in the detection of the areas affected by the landslide, only the pre-event and co-event pairs were used for further analysis.

All results were thoroughly tested statistically using two-tailed t-tests and ANOVA tests. To remove the effect of vegetation from the phase decorrelation (coherence loss), the Normalized Difference Vegetation Index (NDVI) was calculated from Equation (3) within SNAP, based on Sentinel-2 satellite imagery, dated 3 February 2019. This was the closest to the landslides cloud-free and atmospherically corrected image (Level-2A). An NDVI mask was developed in Geographic Information System (GIS) environment and a threshold of 0.2 was used so that all areas with  $NDVI \geq 0.2$  were removed from further analysis. The application of this mask resulted in the calculation of coherence values, which were not affected by vegetation [70].

$$NDVI = \frac{NIR - Red}{NIR + Red} \quad (3)$$

The coherence difference and normalized coherence difference were then calculated from Equations (4) and (5), where  $C_1$  is the coherence from the first image pair and  $C_2$  is the coherence of the second image pair.

$$\Delta C = C_2 - C_1 \quad (4)$$

$$\text{Normalised } \Delta C = \frac{C_2 - C_1}{C_2 + C_1} \quad (5)$$

Their performance in detection between areas affected and not affected by landslides was tested by conducting Receiver Operating Characteristic (ROC) analysis. Lastly, the proposed CCD methodology was validated against another landslide event that took place on 20 February 2019 in the vicinity. The results from the application of the methodology are presented in the following section.

#### 4. Results

The coherence maps along with the coherence histograms were produced after stacking and geolocation, as described earlier, for Sentinel-1A ascending, Sentinel-1A descending, Sentinel-1B ascending, and Sentinel-1B descending SAR interferometric pairs (Supplementary Figures S1, S2, S3, and S4, respectively). The four co-event coherence maps are presented in Figure 10.

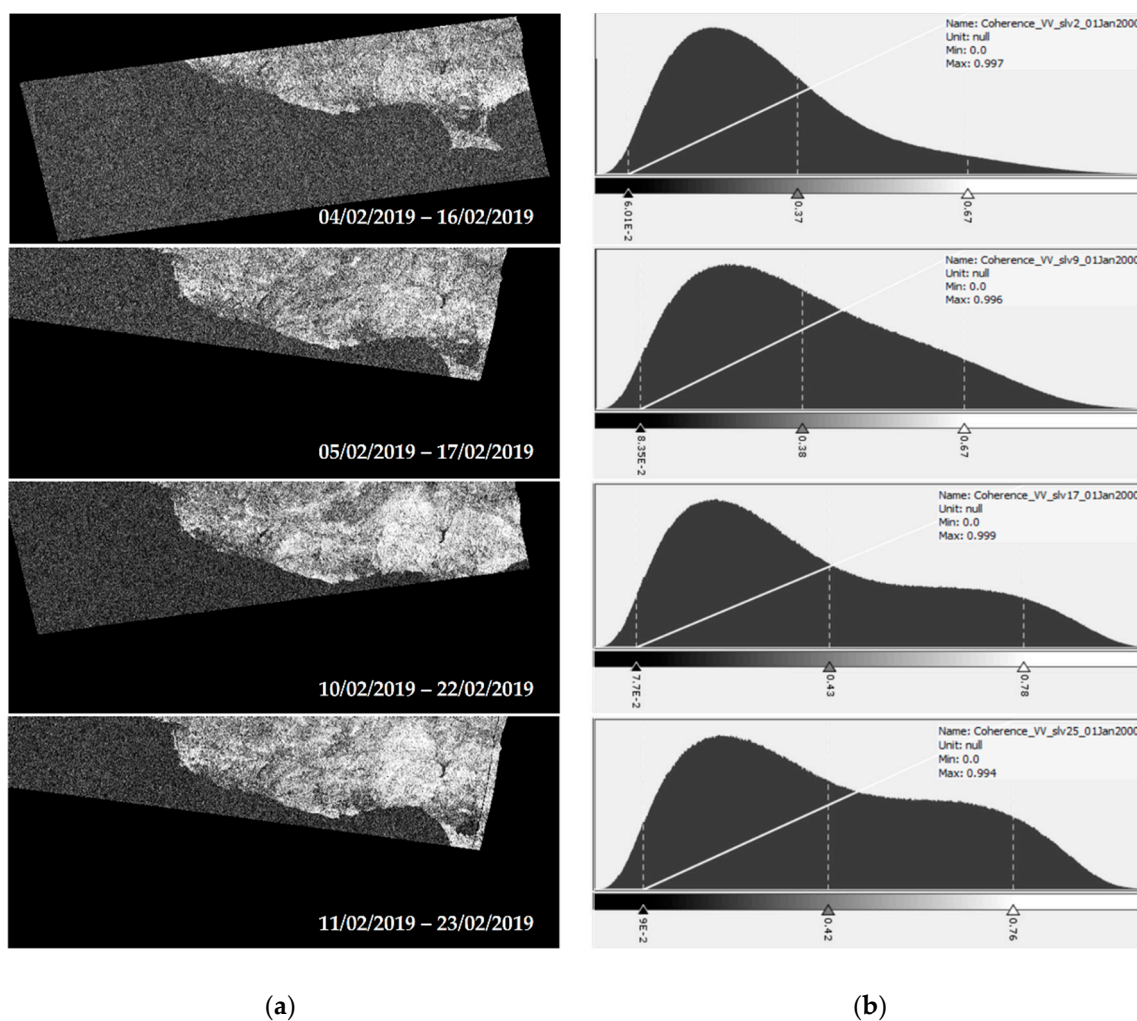


**Figure 10.** (a) Final co-event coherence maps and (b) their respective histograms. The coherence maps produced in SNAP show coherence values ranging from 0 to 1. The coherence maps dated 04/02/2019–16/02/2019 and 10/02/2019–22/02/2019 were developed from Sentinel-1A and 1B ascending images, respectively, whereas the ones dated 05/02/2019–17/02/2019 and 11/02/2019–23/02/2019 were developed from Sentinel-1A and 1B descending images, respectively. The histograms, with coherence on the x-axis and frequency of occurrence on the y-axis, show the frequency of coherence values in pixels at the entire scene.

#### 4.1. Statistical Analysis

A statistical analysis of all results is carried out in the present section. All coherence maps produced in SNAP were inserted in ArcGIS, where the sea was subtracted, and coherence values were classified appropriately for the development of the final coherence products.

Following the instructions by the Cyprus Geological Survey Department, a smaller red polygon was used to define the exact landslide extents, as presented in Figure 11 below, which will be referred to from now on as Area of Interest (AOI). Additionally, the extents of the rehabilitation works were also outlined.

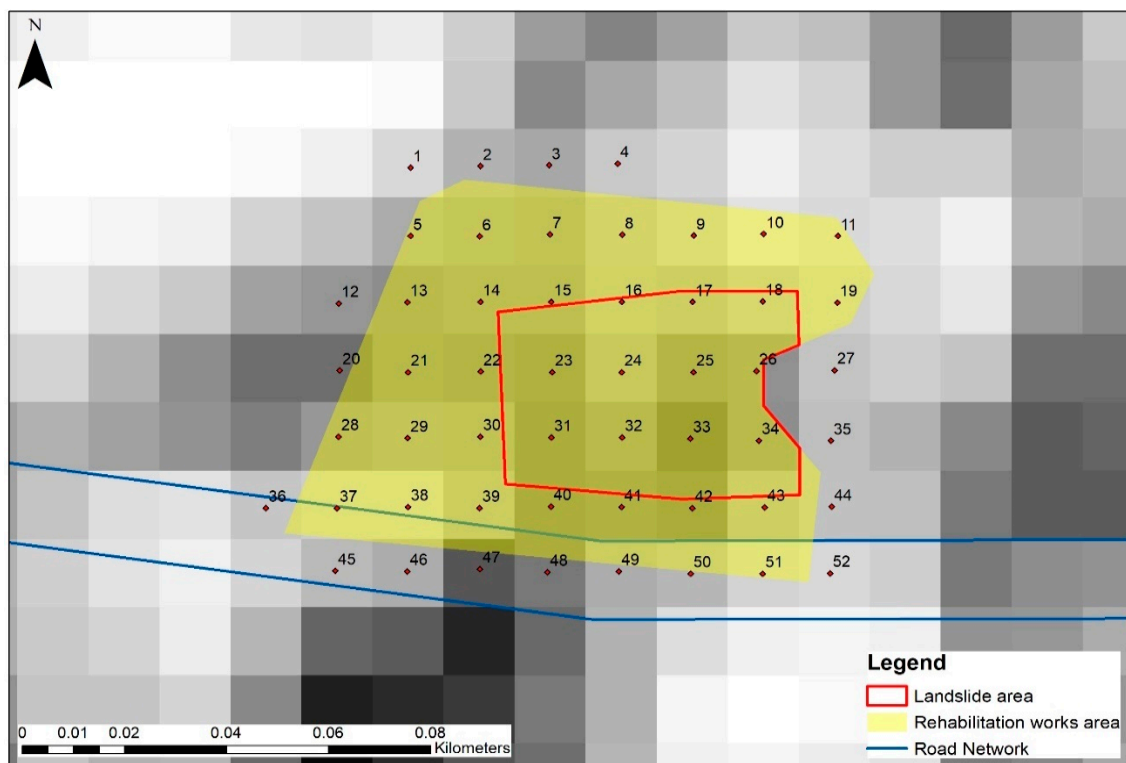


**Figure 11.** Coherence map—Point grid. The entire area where rehabilitation works took place (in yellow) consists of 52 pixels, 20 of which lie within the boundaries of the area affected by the landslide.

For the analysis of the data, a grid of 52 points (Figure 11) was created within ArcGIS, which covers the entire area where rehabilitation works took place (in yellow), starting one day after the landslide occurred, i.e., 16 February 2019, and finishing when the road was opened again to the traffic on 23 March 2019. From these 52 points, 20 points (pixels) lie within the boundaries of the area affected by the landslide (AOI).

From an overview of the findings, it was clear that the coherence values changed more significantly within the landslide area than in the wider area of rehabilitation works. Additionally, the average, minimum, and maximum values were generally lower within the Area of Interest (AOI). Averaging the coherence results as per satellite and satellite pass direction has provided valuable input and reduced the variations that existed when studying the values individually.

A noteworthy observation was that coherence values of pixels located at the boundaries of both areas and were included partially within them, have affected the results of the analysis, but not greatly, as their impact was minimized by averaging observations from different satellites and satellite pass directions.

The results obtained from the interferometric SAR pairs were then averaged for each period by using the coherence values from those with images that were obtained during the specific periods of the event timeline, as seen earlier in Figure 9. Therefore, for Sentinel-1A ascending image pairs, the average of the coherence values obtained from pairs 11/01/2019–23/01/2019 and 23/01/2019–04/02/2019 was calculated, and this value will correspond to the coherence of the pre-event period based on Sentinel-1A

ascending observations. The same was performed for the remaining SAR acquisitions, and the average results for Sentinel-1A and 1B ascending and descending based products are presented in Figure 12.



**Figure 12.** Coherence changes in the three periods for (a) the entire area and (b) the Area Of Interest (AOI). The minimum, maximum, and average coherence values obtained from Sentinel-1A and 1B ascending and descending based products as well as the overall average coherence values (min, max, and average) are presented during the pre-event, co-event, and post-event periods.

The trend of the changes in coherence over time in average, minimum, and maximum values was similar after averaging the coherence values from all SAR pairs. This finding was intensified in the case of the Area Of Interest (AOI) where all three sets of values follow identical trends. At the same time, this led to a reduction of the range of values, i.e., the difference between maximum and minimum values, especially in the case of the confined area of the landslide.

From the above, it is clear that both Sentinel-1A and Sentinel-1B satellites seem to be able to identify the sudden coherence loss, i.e., the phase decorrelation, from the pre-event to the co-event period, and the increase in coherence values between the co-event and post-event period. The average coherence values for the three periods, based on observations from all satellites and satellite pass directions for the wider area (rehabilitation works) are shown in Figure 13.

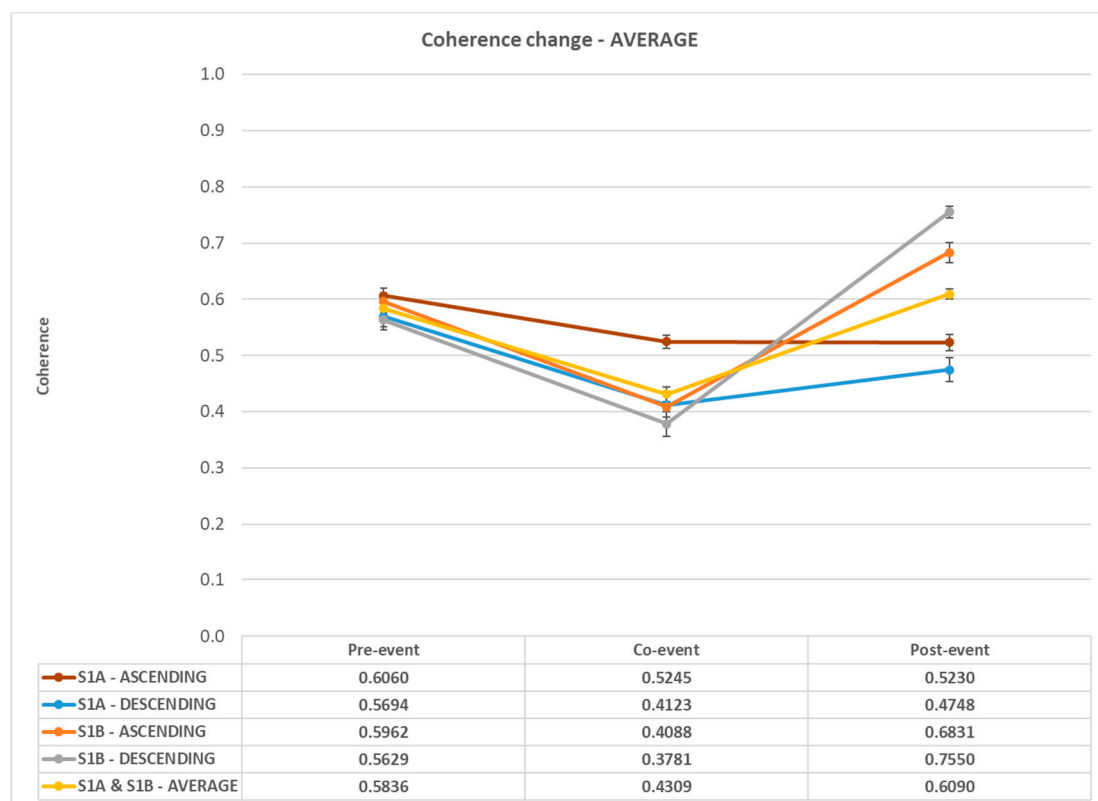


**Figure 13.** Average coherence changes in the wider area of rehabilitation works.

From the figure above, the decorrelation (coherence loss) between the pre-event and co-event periods and the coherence gain between the co-event and post-event periods become more clear. In fact, in Sentinel-1A ascending based interferometric pairs, coherence decreased by 13.4% from 0.606 to 0.525 between the two periods and remained stable between the co-event and post-event periods. In the case of Sentinel-1A descending pairs, average coherence decreased significantly from 0.569 to 0.412 (−27.6%) and then increased by 15.2% from 0.412 to 0.475.

In the case of Sentinel-1B ascending image pairs, average coherence was 0.596 during the pre-event period and dropped by 31.4% and reached its minimum value of 0.409 during the co-event period. Then it raised significantly by 67% during the post-event period reaching its maximum value of 0.683. For Sentinel-1B descending image pairs, average coherence decreased by 32.8% from 0.563 during the pre-event period to 0.378 (minimum value) within the co-event period. Average coherence then almost doubled (+99.7%) between the co-event and post-event periods reaching its maximum value of 0.755.

Therefore, interferometric pairs from Sentinel-1B imagery appear more efficient, compared to Sentinel-1A, in demonstrating the coherence loss between pre-event and co-event periods and the coherence gain from co-event to post-event periods. This is due to the fact that, in the case of

Sentinel-1B imagery, minimum average coherence values are found in the co-event period, whereas, in the Sentinel-1A-based interferometric pairs, minimum average coherence values lie within the rehabilitation works period. The average coherence continues to decrease at a rate of 22.5% and 13.7% during the period of rehabilitation works for ascending and descending pairs respectively. This, in turn, leads to their inability to present the maximum coherence loss and gain between the periods under study.

This problem seems to be minimized when averaging all results together. In this case, average coherence starts at 0.584 during the pre-event period and then decreases by 26% towards the co-event to a value of 0.431. This value is not the minimum, as it continues to decrease by another 8.4% reaching its minimum 0.395 during the rehabilitation works period. However, the earlier issue is mitigated by a significant increase of 41.3% between the co-event and post-event periods.

Within the determined landslide area, coherence loss and gain trends appeared to be strengthened, as presented in Figure 14. For Sentinel-1A ascending pairs, average coherence starts at 0.563 during the pre-event period and reaches 0.473 during the co-event period (−15.9%). Then, it increases by 16.9% and reaches 0.523 at the post-event period. In the case of Sentinel-1A descending, the situation is similar, as coherence decreased by 16.5% between the pre-event (0.518) and co-event periods (0.432) and then increased by 16.3% and reached 0.527. In both cases, the increase and decrease in coherence look symmetrical. As before, the minimum average values are not within the co-event period as values appear to decrease even more during the rehabilitation works.

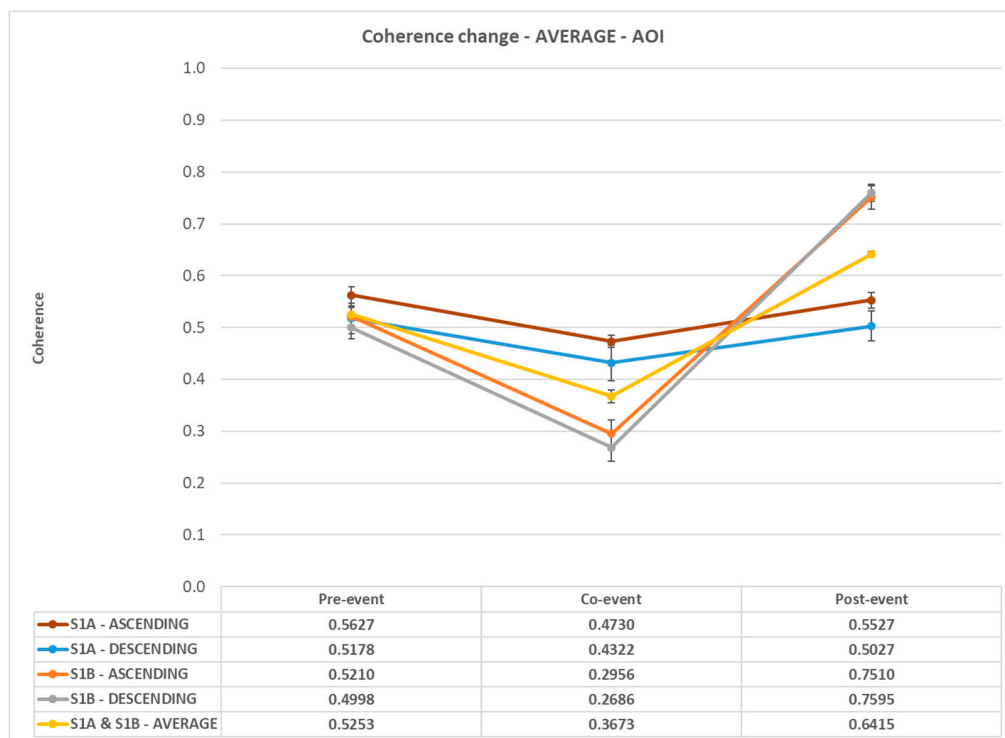


**Figure 14.** Average coherence changes within the boundaries of the Area Of Interest (AOI).

In the case of Sentinel-1B ascending pairs, there is a significant coherence loss of 43.3% between the pre-event (0.521) and co-event (0.296) periods. Then, from its minimum value, it increases by a substantial 154.1% to reach its maximum value of 0.751 during the post-event period. The average coherence values for the Sentinel-1B descending pairs follow similar coherence changes as in the previous case. In fact, average coherence starting at 0.500 before the landslide, decreases by 46.2% and reaches its minimum value of 0.269 during the co-event period. Then it increases by a vast 182.7% and reaches its maximum value of 0.760 after the road opened to traffic.

The averaging of the results within the AOI show a decrease of 30.1% in coherence between the pre-event (0.525) and co-event pairs (0.367) and an increase of 74.6% between the co-event and

post-event pairs, which reached a maximum value of 0.642. The main difference is that the minimum value of average coherence is during the co-event period and not during the rehabilitation works, as in the case of the average for the wider area. This finding is very promising, as it provides a clear distinction between the landslide and rehabilitation works area.

Analysis of variance (ANOVA) statistical tests and two-tail t-tests were carried out to prove the statistical significance of the results using a 95% level of confidence. T-tests were used to determine if there is a significant difference between the means of two samples, i.e., time periods, based on a null hypothesis that the means of two populations are equal. The vast majority of the results rejected this null hypothesis, with t values calculated, being outside the predefined limits set by the level of confidence. However, there was one exception in the wider area, regarding the Sentinel-1A ascending pairs between the co-event and post-event period datasets. Within the AOI, there were two cases between the pre-event and post-event datasets for Sentinel-1A ascending and descending pairs that failed to reject the null hypothesis.

Moreover, ANOVA tests were performed to test the null hypothesis that the means of several populations are all equal for the data corresponding to the wider area and the landslide area. The only case that marginally failed in the ANOVA tests were the coherence value datasets obtained from Sentinel-1A descending pairs within the landslide area. This fact is also supported by the results of the t-tests presented above.

These results are well supported from the findings of the analysis that was carried earlier concluding in Figures 13 and 14. The observed variations between the average coherence values between the specific periods were not great enough to assume that the results differ significantly. In the case of Sentinel-1A ascending interferometric pairs, average coherence values in the wider area between the co-event and post-period were almost identical, i.e., 0.525 and 0.523, respectively. Concerning the landslide area, average coherence values, in the case of Sentinel-1A ascending pairs, were similar in the cases of pre-event (0.563) and post-event periods (0.553). The same case is with Sentinel-1A descending pairs since pre-event and post-event average coherence values were very close (0.518 and 0.503). In all cases, these findings do not limit the use of Sentinel-1A pairs, as results are compared between consecutive time periods and, more importantly, between the pre-event and co-event periods in the landslide event timeline.

#### 4.2. Coherent Change Detection Analysis—Landslide Detection

The coherence maps were developed by averaging the consecutive pre-event pairs for each satellite and satellite pass direction. Coherence maps were produced for the two time periods for each satellite and satellite pass direction, as seen in Figure 15. Average coherence maps were also produced as presented in Figure 16.

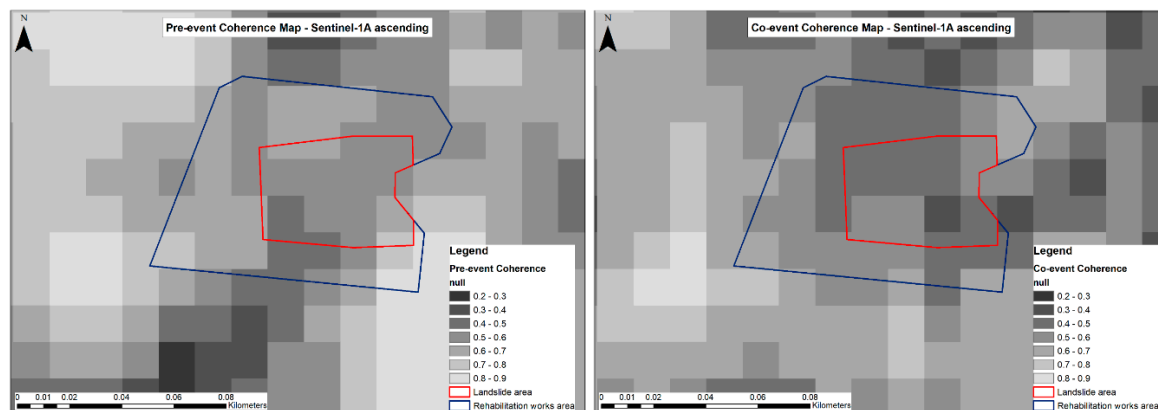
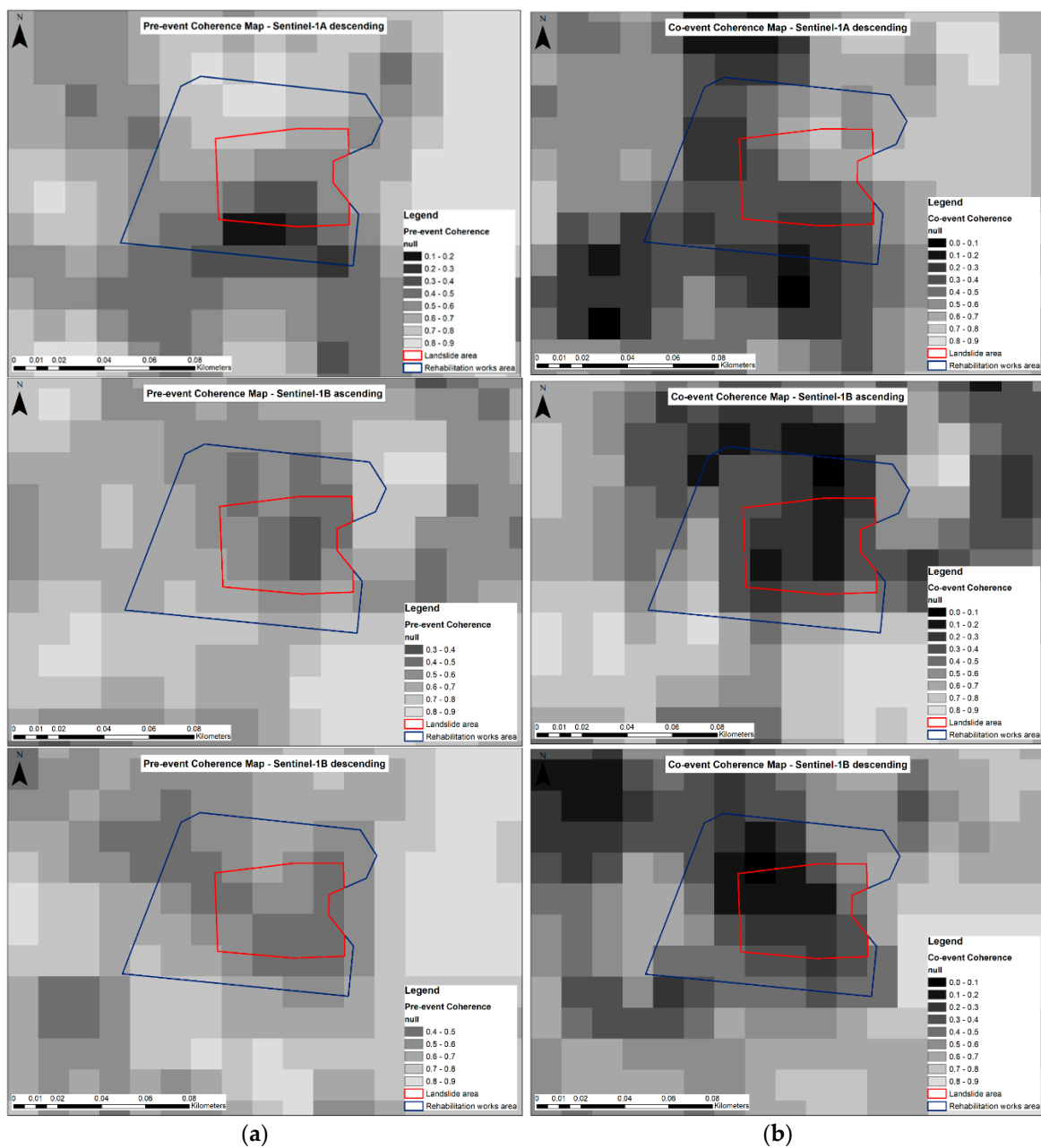


Figure 15. Cont.





**Figure 15.** (a) Pre-event and (b) co-event coherence maps—Sentinel-1A ascending (first), Sentinel-1A descending (second), Sentinel 1-B ascending (third), and Sentinel-1B descending (fourth).

From the first view of the produced maps, Sentinel-1A based coherence maps appear to have misinterpreted the impact of the landslide under investigation. For Sentinel-1A ascending SAR pairs, there was minimal coherence loss between the pre-event and co-event periods, whereas, in the case of descending images, the area with coherence loss appear towards the south and west from the defined landslide area. There appears to be a better representation of the landslide impact in the Sentinel-1B based products with the coherence dropping in the co-event period. The average maps provided similar results. However, to distinguish between coherence loss due to the landslide under investigation and natural coherence loss due to the temporal baseline of SAR images, all the above maps were further compared.

The distinction between coherence changes due to geological hazards and coherence changes due to natural variations was attempted by calculating the coherence change differences, and normalized coherence differences between the pre-event coherence and co-event coherence.

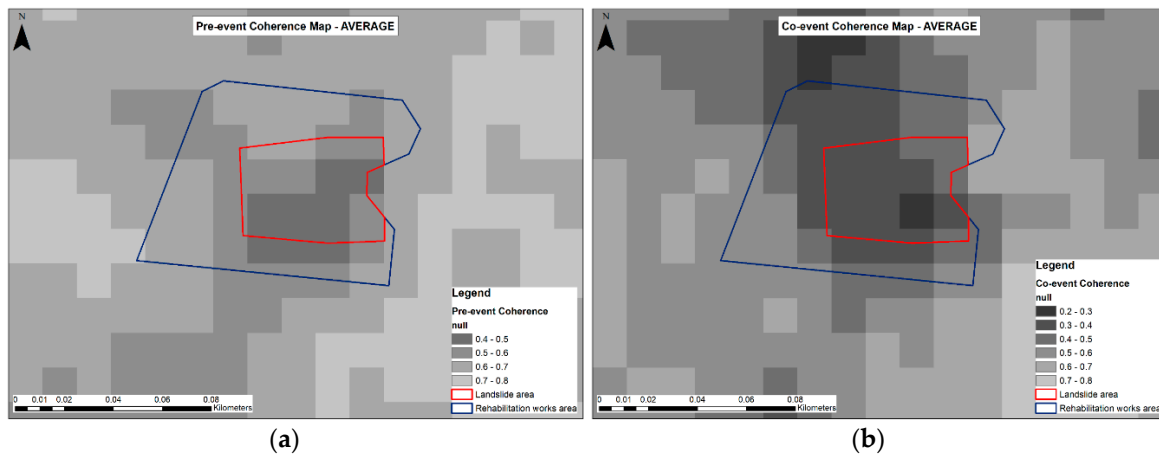


Figure 16. (a) Pre-event and (b) co-event average coherence maps.

Both approaches are based on the assumption that the phase decorrelation caused by geo-hazards is stronger than the phase decorrelation induced by natural temporal changes. This is intensified by using multi-pass SAR imagery with identical and short temporal baselines for all interferometric SAR image pairs. The selection of SAR pairs of 12 days apart assists in ruling out significant nature-derived phase decorrelations. In fact, Sentinel-1 SAR takes full advantage of the long-term coherence, the frequent revisit, the small baselines, and the dual polarisations [57].

Significant changes of coherence must be identified in order to distinguish between a natural coherence decrease and a coherence decrease due to a natural disaster. A perfect relationship between two consecutive images is represented by a coherence value of 1. Thus, in areas where no significant change occurred, a coherence difference and a normalized difference should have zero values. This is never the case as natural decay takes place with coherence values decreasing over time. The distinction between the coherence loss due to the landslide under investigation and the natural coherence loss due to the temporal baseline of SAR images was further enhanced by calculating the expected natural reduction in coherence, as presented in Figure 17.

This was calculated by developing coherence maps, using a single SAR image as a master and the rest of the images as slaves for each satellite and pass direction separately. The coherence maps produced were stacked together and geolocated, so that results can be correctly combined. Then, the coherence maps developed from SAR images, which were both acquired during the pre-event and post-event periods, were used to calculate the average coherence values at the wider area. During these two periods, no known landslides, earthquakes, or other land movement inducing phenomena occurred. There seems to be a natural decay in coherence values in the order of 3.25% every 12 days (Figure 17). Thus, any coherence reduction lower or equal to this threshold was considered normal and all other coherence changes over 3.25% were considered significant.

Moreover, since the area of interest is surrounded by vegetation, which can lead to phase decorrelation, the impact of vegetation was minimised by using satellite images with short temporal baselines (12 days). However, to test the efficiency of the methodology in non-vegetated areas, a coherence mask ( $NDVI < 0.2$ ) was applied to all products in Geographic Information System (GIS) environment. The coherence mask was developed in SNAP software (Figure 18) using a Sentinel-2 image as described in the Materials and Methods section. Additionally, sea was also removed from all layers in order to calculate mean values and standard deviations more accurately.

All results obtained from the application of the two indicators were classified, in ArcGIS, to highlight the possibility for the occurrence of a landslide in the case study site. The classification was based on the mean value and the standard deviation of each dataset.

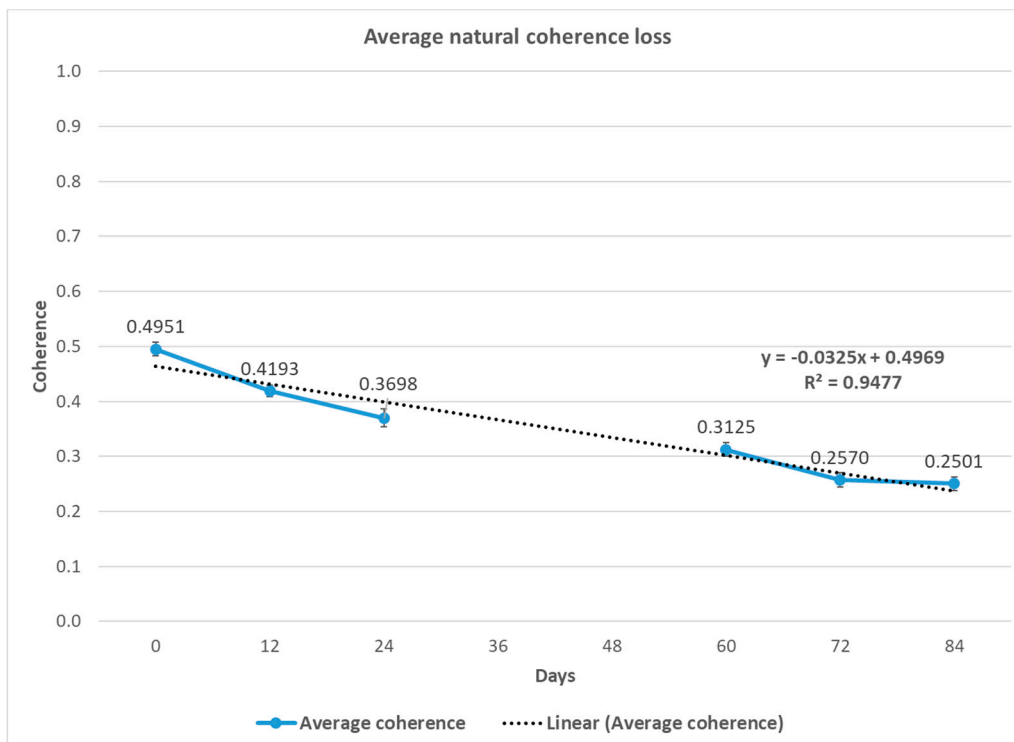


**Figure 17.** Natural coherence loss. Coherence, ranging from 0 to 1 is on the y-axis, whereas the days since the date of the first SAR acquisition are on the x-axis.

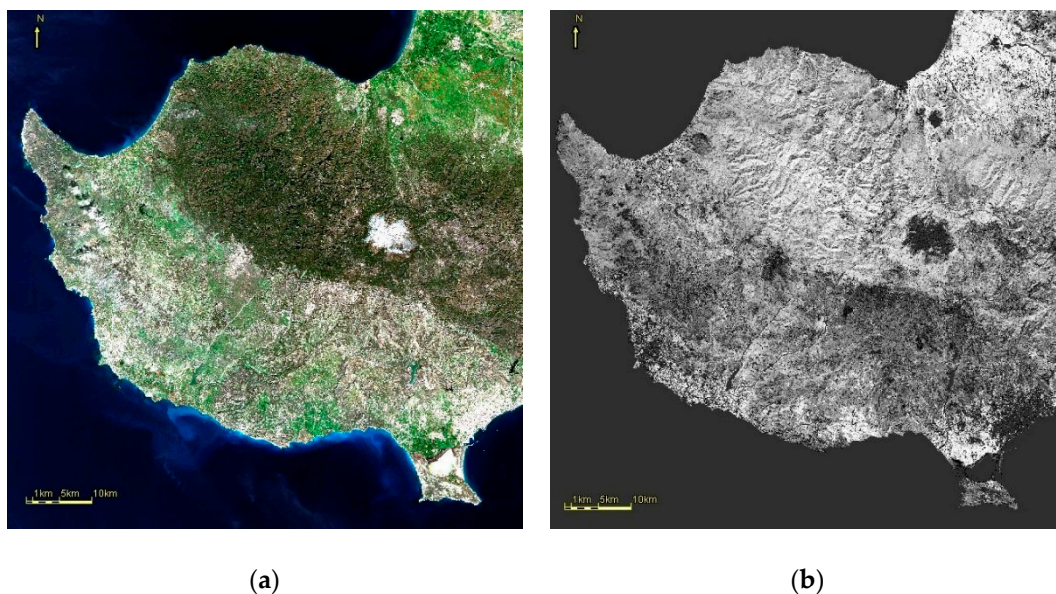


**Figure 18.** (a) RGB of Sentinel-2 image and (b) NDVI mask developed in SNAP software.

More specifically, areas/pixels with values outside of the confidence lower limits (negative values) for 99.73% level of confidence, i.e., three standard deviations from the mean value, were defined as areas that are very highly probable to be affected by landslide. Coherence difference and normalized difference values between two and three standard deviations from the mean value, i.e., 95.45–99.73% level of confidence, were included in the class “High,” i.e., areas with high probability of landslide occurrence. All values that were within one standard deviation, positive or negative, from each dataset mean value were included in the class named “None—Very Low” along with all other positive values, that indicate a coherence increase, and, thus, they are areas that there is no possibility that

a landslide or any other natural hazard phenomenon took place. In the class “Low—Medium,” the values between one and two standard deviations were entered. The conditions used to classify all values were the following:

$$\text{“Very High”} \leq \mu - 3\sigma \leq \text{“High”} \leq \mu - 2\sigma \leq \text{“Low - Medium”} \leq \mu - 1\sigma \leq \text{“None - Very Low”}$$

where  $\mu$  is the mean value and  $\sigma$  is the standard deviation of each dataset. The final products with the differences and normalized differences of coherence are presented below in Figure 19 for each satellite and satellite pass direction separately. White pixels are in areas that were masked out by applying the NDVI mask for removing the vegetation effect.

The above maps fully support the results of the statistical analysis that was conducted earlier in Section 4.1. The coherence difference and the normalized coherence difference show similar spatial patterns in all four cases individually.

Interferometric pairs from Sentinel-1A ascending and descending images failed to identify the area affected by the landslide. This was pointed out during the statistical analysis, based on the findings from the t-tests and ANOVA tests that were carried out, but also as the minimum coherence values, obtained from Sentinel-1A imagery, that were found within the period of rehabilitations works, which follows the co-event one. More specifically, Sentinel-1A ascending based maps show a small area of high landslide probability at the eastern boundaries of the defined area adjacent to the A6 motorway, by calculating coherence differences, which turns to Low-Medium when the normalized differences were calculated. Sentinel-1A descending-based coherence difference products detected a small area of high landslide probability at the northwest boundaries of the AOI and some smaller areas to the west and southwest of the AOI with high and very high probability for landslides. However, in the case of the false alarm at the area towards the west, this occurs because it is situated within the boundaries of the A6 motorway. These indications were minimized after calculating the normalized coherence differences.

Sentinel-1B satellite appears to perform significantly better in identifying areas that are highly and very highly possible for a landslide to have occurred. The normalized coherence difference maps, based on ascending and descending interferometric SAR pairs, have succeeded to identify the extents of the landslide, confirming in a spatial manner the results of the statistical analysis. In fact, they enhanced the results obtained through the calculation of simple coherence differences by turning areas of low and medium probability to high probability ones and areas of high probability to very high landslide probability. At the same time, they minimized false alarms that were indicated by the simple coherence differences products.

Since all the acquisition and sensor characteristics of the Sentinel-1A and Sentinel-1B satellites are nearly identical, an explanation for this could be the different dates between the co-event SAR acquisitions of the Sentinel-1A and Sentinel-1B, as shown in Table 1. Sentinel-1A images were acquired 10–11 days prior and 1–2 days after the landslide, whereas the Sentinel-1B images are dated 4–5 days before and 7–8 days after the landslide. The difference in dates could have introduced additional phase decorrelations due to the residing meteorological conditions on the specific dates.

Comparing the simple coherence difference and the normalized one, the main distinction between the two detection indicators is that the coherence difference provided many incorrect detections, while the normalized coherence difference has less cases of false alarms. In fact, the normalized coherence difference performed better than the coherence difference in all cases. The coherence difference indicator shows greater changes in areas with originally (pre-event) high coherence values, whereas the normalized coherence difference method adjusts the difference based on the sum of the pre-event and co-event values, i.e., denominator in Equation (5).

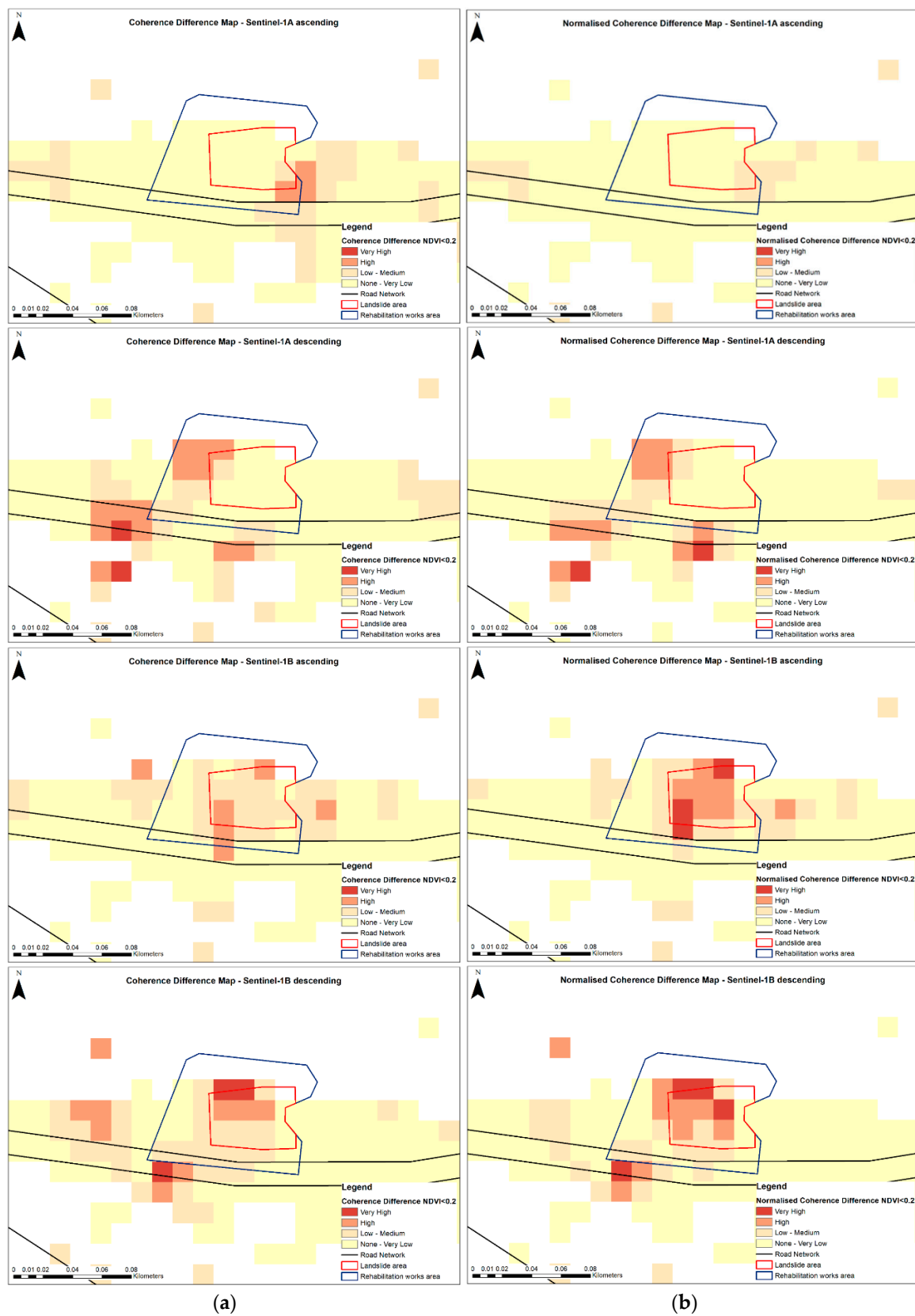


**Figure 19.** (a) Coherence difference and (b) normalized coherence difference maps—Sentinel-1A ascending (first), Sentinel 1-A descending (second), Sentinel 1-B ascending (third), and Sentinel 1-B descending (fourth).

To ensure the efficiency of the proposed CCD methodology, it is very important to keep temporal baselines at an absolute minimum. This condition is satisfied by the Sentinel-1 mission with the very short revisit times it offers. This fact can also assist in the further improvement of the proposed method into a multi-pass CCD methodology for detecting and monitoring natural hazards. In that aspect, average maps of coherence difference and normalized coherence difference were developed, as presented in Figure 20.

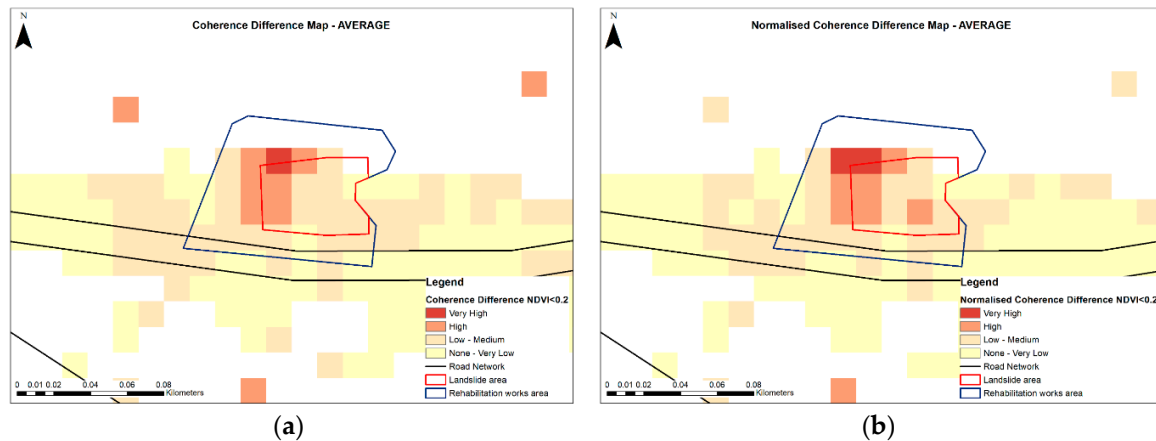


**Figure 20.** (a) Coherence difference and (b) normalized coherence difference maps—Average.

The averaging of all maps provided some valuable input in the benchmarking of the methodology. However, the results were influenced significantly by the poor results obtained by the Sentinel-1A interferometric SAR pairs. There is a better distinction between areas affected and not affected by the landslide, when compared with the Sentinel-1A satellite-based products, but their overall performance is inferior to that of the Sentinel-1B based products.

In that aspect, based on the superior performance of the Sentinel-1B satellite, the results from the coherence difference and normalized coherence difference maps, which were developed by Sentinel-1B ascending and descending image pairs, were utilized to produce Sentinel-1B average coherence difference and normalized coherence difference products, as presented in Figure 21.

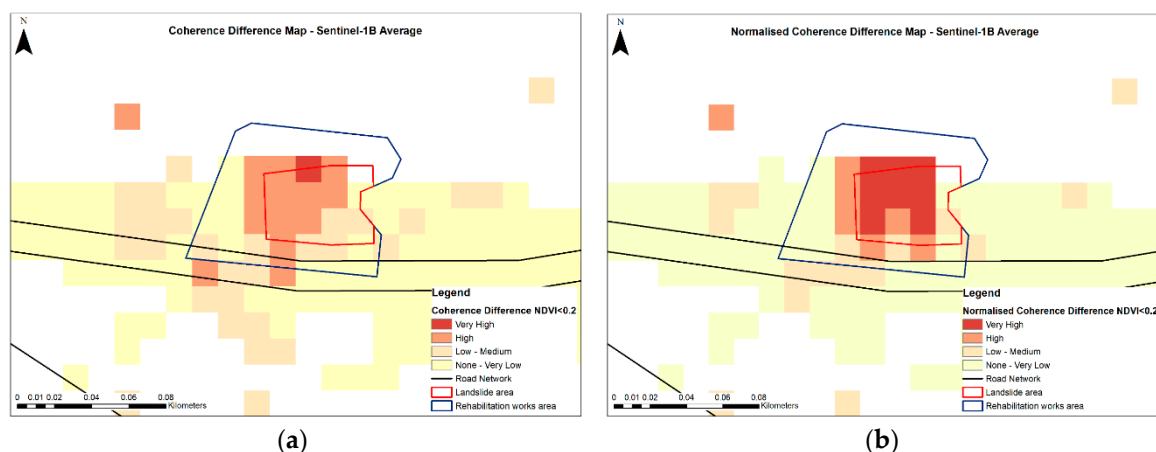


**Figure 21.** (a) Coherence difference and (b) normalized coherence difference maps—Sentinel—1B average.

The averaging of these two products has further improved the previous individual results of the Sentinel-1B ascending and descending SAR pairs, matching the landslide defined area, especially in the case of the normalized coherence difference indicator. The pixels of very high landslide probability almost cover fully the extents of the landslide area.

At the same time, the number of false alarms was reduced when compared to the individual Sentinel-1B ascending and descending based results, with some sparse incidents (single pixels) located to the west and east of the area under study, which is in the majority of cases in the class of “Low—Medium” probability. The few pixels within the motorway boundaries can be removed from the analysis, as most likely the coherence changes are due to the traffic using the A6 motorway on its other direction.

#### 4.3. ROC Analysis

The performance of the coherence difference and normalized coherence difference indicators was further tested for the specific case study, by the Receiver Operating Characteristic (ROC) analysis. ROC analysis has been widely used for the benchmarking of natural hazard detection methods [42,59,71]. A map of landslide and non-landslide pixels is created and the trade-off between the true positive fraction and the false positive fraction with certain thresholds are calculated. In this case, four different thresholds were defined that correspond to the probability classes set for the development of the coherence difference and normalized coherence difference maps.

Then, the true positive fraction (y-axis), i.e., the number of pixels within the landslide area that were detected as a landslide and the non-landslide pixels that were correctly classified as non-landslide pixels, is then plotted against the false positive fraction (x-axis), i.e., non-landslide pixels that were detected as landslide ones and landslide pixels that were detected as non-landslide ones. A good landslide detection indicator is expected to detect true positive pixels faster than false positive ones. Hence, the more accurate the detection indicator is, the closer the ROC curve should lie to the upper left corner of the plot. The ROC curves and the complete statistics from the ROC analysis were calculated using the web-based calculator for ROC curves [72].

In Figure 22, the blue line and red marks represent the fitted ROC curve and the grey lines are the 95% confidence intervals of the fitted ROC curves. The coherence difference performed with an overall accuracy of 93% and the normalized coherence difference with an overall accuracy of 94.8% for detecting the landslide and non-landslide areas. The true-positive rate, which is also known as sensitivity or probability of landslide detection, was 63.2% in the case of the coherence difference and increased to 73.7% for the normalized coherence difference. Lastly, the false-positive rate, or the probability of false alarm, was calculated as “1—specificity”, and, for both indicators, was approximately 1%. The summary statistics calculated for the entire scene (Figure 21), which consists of 115 pixels, are presented in Table 2.

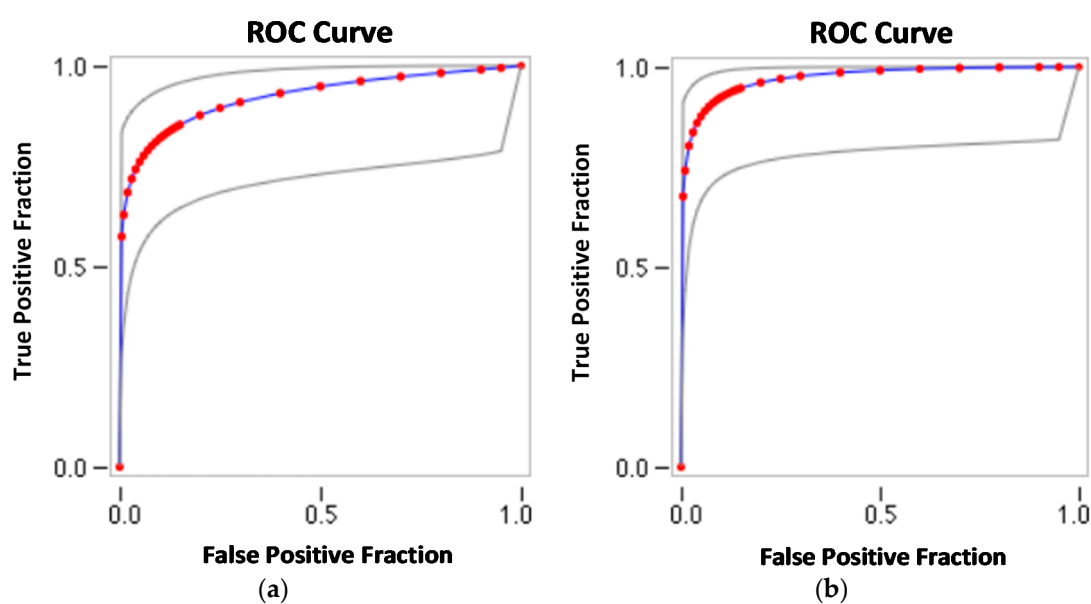


**Figure 22.** Receiver Operating Characteristic (ROC) curves for the (a) coherence difference and (b) normalized coherence difference maps—Sentinel-1B average.

**Table 2.** Receiver Operating Characteristic (ROC) summary statistics.

	Coherence Difference	Normalized Coherence Difference
Number of cases	115	115
Number correct	107	109
Accuracy	93%	94.8%
Sensitivity	63.2%	73.7%
Specificity	99%	99%
Positive cases missed	7	5
Negative cases missed	1	1
Fitted ROC area	0.922	0.972
Empirical ROC area	0.897	0.952

The ROC analysis also proved that the normalized coherence difference performed better than the coherence difference indicator as it can detect the areas affected by landslide more efficiently. The five cases/pixels that were missed by the normalized coherence difference indicators were all at the edges of the area of interest and the majority of those lie only partially within it, which causes their wrong characterization as pixels of none-very low and low-medium landslide occurrence probability, as described earlier.

In conclusion, the multi-pass Coherent Change Detection (CCD) methodology, through the application of the normalized coherence difference indicator, based on averaging Sentinel-1B products, proved to be the most beneficial for the detection of landslide phenomena and their impact on critical infrastructure. It is the first time that this methodology is applied in the case of landslides induced by heavy rainfall.

The validation of the above proposed methodology follows in the next section of the study, using another landslide event that occurred on 20 February 2019, by the old Paphos—Limassol road near Petra tou Romiou as the validation site.

#### 4.4. Validation of Methodology

The performance of the multi-pass CCD methodology applied was tested at another case study site, affected by a landslide, following heavy rainfall. The landslide event took place on 20 February 2019 causing structural issues, that led to the closure of a 3-km long part of the old road from Paphos to Limassol, approximately 200 m away from “Petra to Romiou”, which remains closed until today for security reasons. The extensive precipitation and residing soil erosion issues were found to be the main reasons for this phenomenon. To date, the access from Paphos to Limassol is carried out only via the Paphos—Limassol motorway A6.

Since this case study was used for validation purposes, no intermediate steps are analyzed within the present section. Therefore, the final coherence difference and normalized coherence difference results produced from the various Sentinel-1 datasets using the CCD methodology are presented below. The present landslide was not well documented by the local authorities, so the landslide extents were approximately defined after a site visit. The coherence difference and normalized coherence difference maps are presented in Figure 23.

From a first overview of the above maps, it is noticeable that both Sentinel-1A and Sentinel-1B satellites in their ascending pass successfully detected the landslide under study, whereas descending pass satellites failed to identify the areas affected by the landslide.

This was due to the fact that the landslide occurred at a slope facing in the southwest direction, which enables satellites of the ascending pass direction to acquire geometrically correct images and avoid shadow and/or overlay effects that can be introduced in the processing due to the topography of the area with the residing steep slopes.



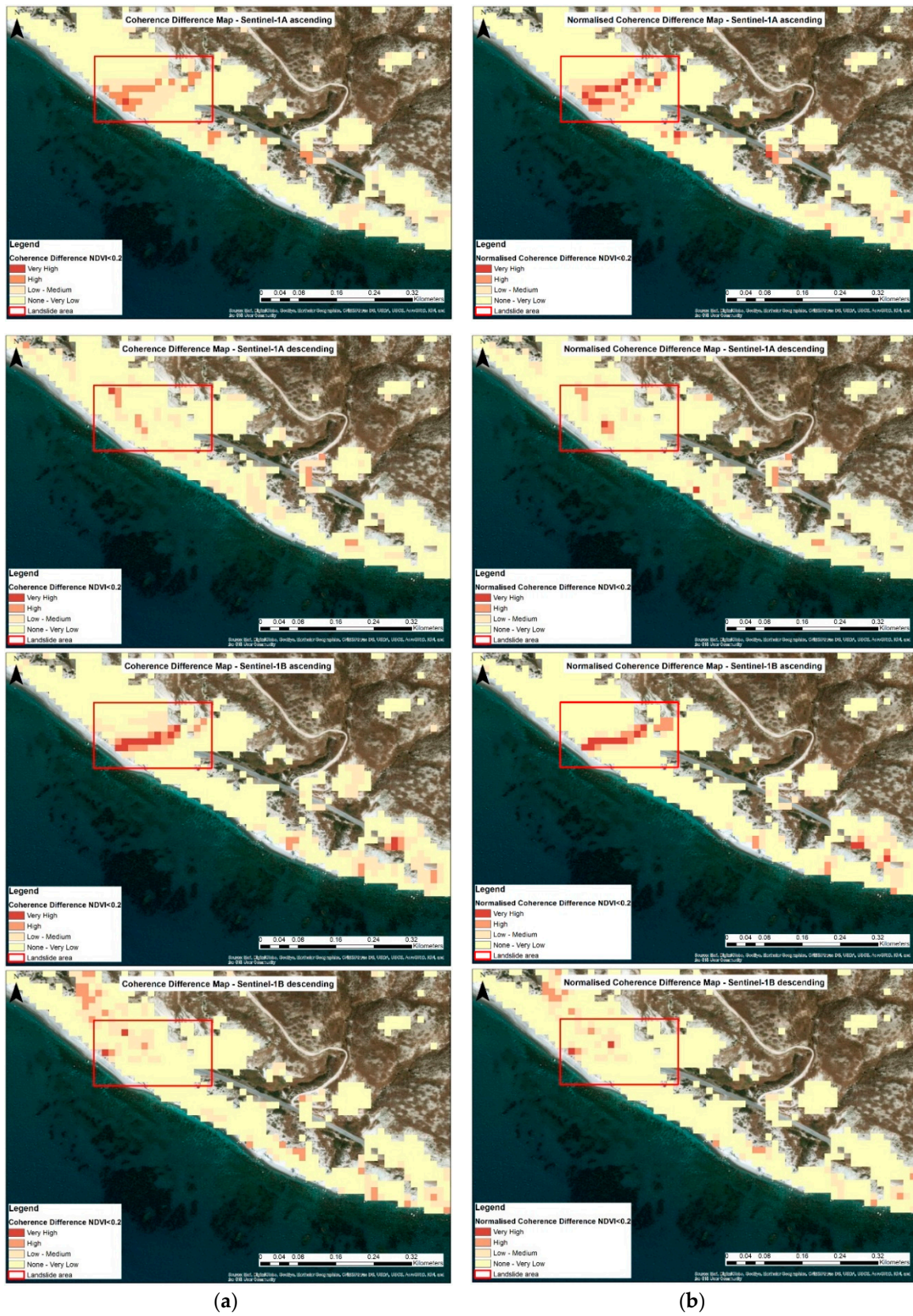


**Figure 23.** (a) Coherence difference and (b) normalized coherence difference maps—Sentinel-1A ascending (first), Sentinel-1A descending (second), Sentinel 1-B ascending (third), and Sentinel-1B descending (fourth).

Moreover, the ascending pass satellites detected some areas of high and very high probability of landslide occurrence to the southeast of the study area. Although some of these areas are within the boundaries of the old Paphos—Limassol road, some others, especially from the level of the road downslope towards the sea, are noteworthy. Since one of the main reasons for this landslide was the residing soil erosion issues, there might be additional areas that were eroded and collapsed or subsided following the heavy rainfall.

In all cases, the normalized coherence difference indicator managed to detect more successfully the areas affected by the landslide by providing fewer false alarms. In fact, the majority of the false indications fall within the road boundaries, which is a matter that could have led to a loss of coherence since traffic was present during the acquisition dates of the images used as “master” during the interferometric processing.

The average coherence difference and normalized coherence difference maps were also developed, as presented in Figure 24, to study the impact of the landslide further by taking advantage of the short revisit times of the Sentinel-1 satellites.

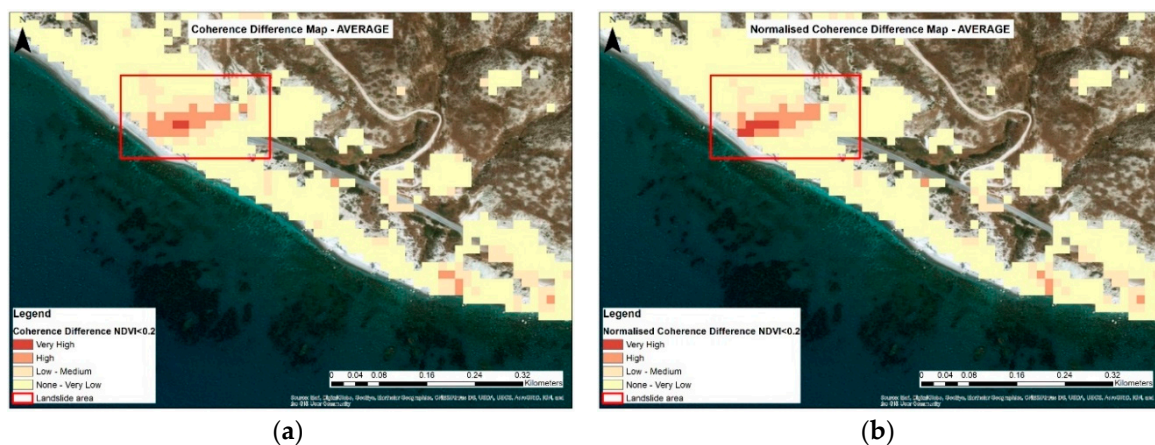


**Figure 24.** (a) Coherence difference and (b) normalized coherence difference maps—Average.

The averaging of all results resulted in improved and more accurate end-products compared to the individual Sentinel-1A and Sentinel-1B based ones. The average coherence difference and normalized coherence difference products show the extents of the area affected by the landslide whereas, at the same time, managed to nearly eliminate all false indications that were located on the old Paphos—Limassol road. Moreover, the area to the southeast of the landslide is now highlighted partially as an area of high landslide probability in both maps, as presented above.

The further optimization of the detection results was attempted by combining the results of the two successful products based on ascending Sentinel-1A and Sentinel-1B imagery, as it was performed earlier for the case study near Pissouri. Based on the superior performance of both satellites in the ascending pass direction, the results from the coherence difference and normalized coherence difference maps, which were developed earlier, were averaged to produce Sentinel-1A and Sentinel-1B average coherence difference and normalized coherence difference products, as presented in Figure 25.

Once more, this combination resulted in the further improvement in landslide detection providing a clear representation of the area affected by the landslide and minimized the false indications by limiting to those located along the old Paphos—Limassol road in the case of the normalized coherence difference map.

The averaging of the two products based on ascending Sentinel-1 imagery, i.e., S1A and S1B, has further improved the previous results that were based on individual satellite observations, which optimized the detection of the area that was affected by the landslide (very high probability), especially in the case of the normalized coherence difference indicator.

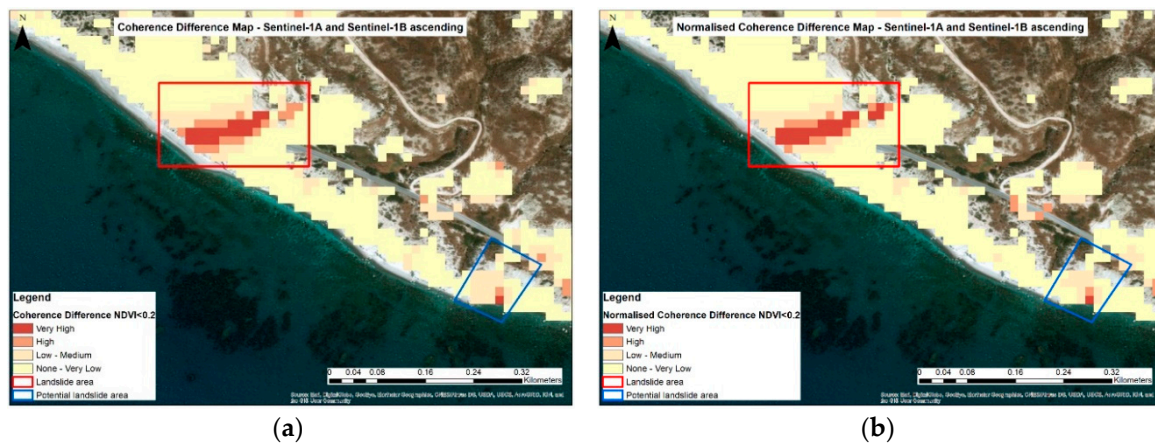


**Figure 25.** (a) Coherence difference and (b) normalized coherence difference maps—Sentinel 1-A and Sentinel-1B ascending average.

Other areas marked with high probability are all along the road and are not taken into consideration, with the exception of the area to the southeast of the AOI, where the values mostly fall into the “Low—Medium” class with some areas of high and very high probability of landslide occurrence, downhill toward the sea. As seen in Figure 25, this area was marked as a site that was potentially affected by a landslide.

The normalized coherence difference has once more performed better than the coherence difference indicator, as happened in the case of the landslide by A6 motorway near Pissouri, providing more accurate results for detecting the area affected by a landslide and less number of false indications regarding the occurrence of a landslide.

## 5. Discussion

Landslides are considered as one of the most devastating natural hazards worldwide. They are triggered by many factors that can be monitored via ground-based or satellite-based techniques. Conventional ground-based geodetic, photogrammetric, geophysical, and geotechnical techniques are being used for many decades for monitoring the geological stability and other parameters that can induce land displacement events. These techniques involve very extensive, time-consuming, and costly field surveys and the use and/or installation of expensive instrumentation. They are usually conducted only at specific areas with proven history in hazardous events since monitoring networks are difficult and costly to be established everywhere.

Space-based passive and active remote sensing techniques, utilizing optical and radar images respectively, are widely used in many applications and research fields, as they are very efficient in monitoring changes on the Earth’s surface. The continuously improving spatial and temporal characteristics of the satellites, and the capabilities to acquire images day and night and under all weather conditions as in the case of SAR images, have laid the ground for continuous monitoring of land and sea. This, in fact, is enhanced through the complementarity of datasets that the various satellite missions provide. In recent years, the Earth Observation (EO) sector has provided remarkable opportunities for the monitoring and assessment of critical infrastructure resilience.

There seems to be a complementarity of the different monitoring techniques, as they provide different kind of information. Therefore, the integration of EO-based derived data with all available information on ground deformation collected through other in-situ techniques, is the way forward to achieve accurate and continuous monitoring and mapping of land displacement, and reliable assessment of the impact of natural hazards to infrastructure.

The Coherent Change Detection (CCD) methodology (Figure 26) can operate complimentary with other EO-based techniques, such as DInSAR, or as a stand-alone technique for monitoring ground deformations over large areas providing useful information, of qualitative nature, regarding the impact

of a natural hazard. Its advantage compared with the DInSAR methodology is the fact that the processing time required is limited, which provides valuable information very quickly to responsible local authorities.

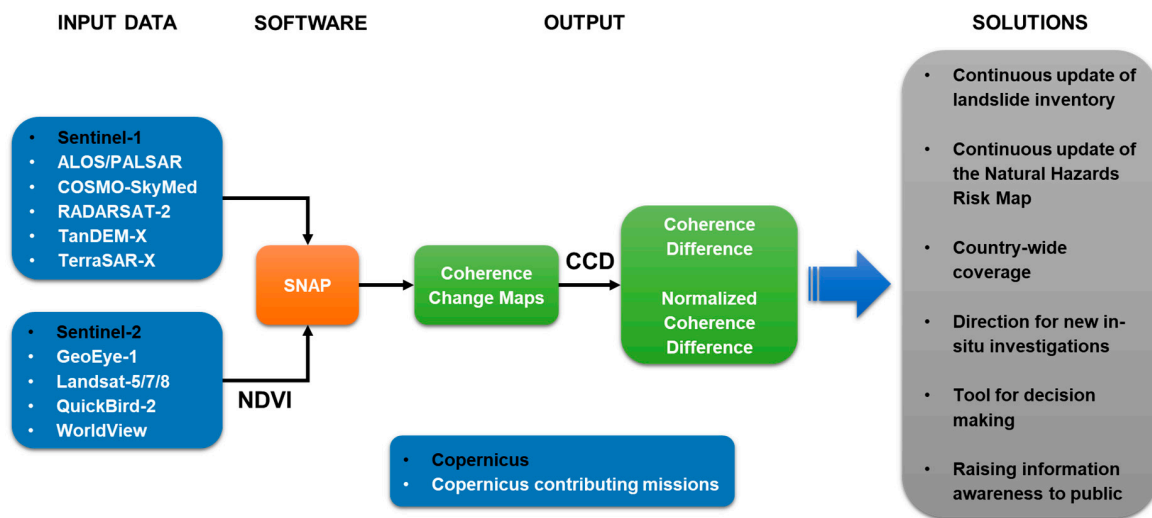


**Figure 26.** The Coherent Change Detection (CCD) methodology and the solutions that it can offer.

Additionally, CCD techniques, using the advantages of Sentinel-1 satellites and other contributing missions, can be used for the continuous monitoring of geo-hazards assisting in the update of natural hazard risk maps and geological suitability maps by detecting areas affected by natural hazards, such as landslides, with great accuracy. CCD methodology can provide valuable input for the extents of the affected area and can even detect landslides that occurred in remote areas and were not recorded before. It was the first time that such a technique has been successfully applied for landslides induced by heavy rainfall.

The contributions of the Copernicus program through the freely available Sentinel-1 and Sentinel-2 satellite data along with the open-source software SNAP provided freely by the European Space Agency (ESA), which can be used to process the Copernicus data, can lead to the collection of valuable information in a timely manner due to the high temporal resolution and multi-pass nature of the Sentinel satellites.

It is worth noting that the Coherent Change Detection (CCD) technique can be used at two different stages by producing different types of outputs. At the first stage, CCD can provide an initial assessment of the impact due to the occurrence of a natural hazard very quickly, using a minimum number of three SAR images and creating two interferometric SAR pairs including one pre-event and one co-event pair. Lastly, CCD can develop more accurate end-products, showing the exact extents of the natural hazard affected area through the exploitation of the multi-pass advantages of the Copernicus Sentinel-1 mission and combining numerous pre-event and co-event SAR imagery.

## 6. Conclusions

The application of the proposed CCD methodology provided valuable information for the location of the area that was affected by the landslide through the study of the normalized coherence difference between two sets of interferometric SAR pairs including a pre-event and a co-event one. Its application proved that the phase decorrelation caused by a natural disaster is far more significant than the one caused by the natural coherence loss due to the temporal baseline of two or more consecutive SAR images.

The results from the application of the CCD methodology in the case study near Pissouri and its validation through the successful detection of two other landslides in the area near Petra tou Romiou proved that this methodology can provide significant information for the coordination of emergency

response services and other responsible authorities in limited time. Additionally, it can provide directions for carrying out new site-specific investigations. It was the first time that this methodology was applied successfully for detecting natural hazards induced by intense precipitation.

Based on the thorough analysis that was carried out in the present paper, the proposed methodology has proven to be efficient in the detection and monitoring of landslides as well as for assessing their impact on infrastructure. Despite the fact that the results are not quantifiable, as in the case of DInSAR methodology, CCD methodology provides valuable input for the extents of the affected area and can even detect landslides that occurred in remote areas and were not recorded before. It was the first time that such a technique has been successfully applied for landslides induced by heavy rainfall.

The provision of information about an upcoming hazard in a timely manner is of vital importance, when lives are in danger. There is an emerging need for real-time and/or near real-time monitoring systems, which are known as Early Warning Systems (EWS). To achieve real-time and/or near real-time monitoring, the entire process from data acquisition to the release of the warning must be fully automated for a real-time hazard assessment.

With the proposed CCD methodology, products can be developed at two stages. The first stage with quick products that can be developed based on the normalized coherence difference calculation by using three SAR images, i.e., two before and one after the natural hazard occurrence. These can provide an initial assessment of the impact of the natural disaster, which is valuable information for the coordination of emergency response services and for raising information awareness to the public.

Lastly, at the second stage, CCD can develop more accurate multi-pass end-products, showing the exact extents of the natural hazard affected area through the exploitation of the multi-pass advantages of the Copernicus Sentinel-1 mission, combining numerous pre-event and co-event SAR imagery. These second stage products can be used for the continuous update of the landslide inventory and natural hazard risk map as well as to provide directions for carrying out new site-specific investigations.

Since the selection of the type of SAR imagery is case-specific, different combinations of SAR sensors are planned to be tested for applications at different areas to achieve optimum results. More specifically, the proposed CCD methodology is planned to be tested by exploiting longer wavelength SAR acquisitions, such as L-band and P-band, for applications at areas covered with vegetation and higher resolution SAR products, such as those produced by the TerraSAR-X and COSMO-SkyMed missions for the establishment of an Early Warning System in Cyprus.

**Supplementary Materials:** The following are available online at <http://www.mdpi.com/2072-4292/12/10/1560/s1>. Figure S1: Coherence maps—Sentinel-1A ascending. Figure S2: Coherence maps—Sentinel-1A descending. Figure S3: Coherence maps—Sentinel-1B ascending. Figure S4: Coherence maps—Sentinel-1B descending.

**Author Contributions:** Conceptualization, M.T. Methodology, M.T., C.D., and D.G.H. Software, M.T. Validation, M.T. Formal analysis, M.T. Investigation, M.T. and C.D. Resources, M.T. and C.D. Data curation, M.T. and C.D. Writing—original draft preparation, M.T. Writing—review and editing, M.T., C.D., and D.G.H. Visualization, M.T. Supervision, C.D. and D.G.H. All authors have read and agreed to the published version of the manuscript.

**Funding:** This research received no external funding.

**Acknowledgments:** The authors would like to acknowledge the “CUT Open Access Author Fund” for covering the open access publication fees of the paper. The authors would like to express their appreciation to the Geological Survey Department of Cyprus for their continuous support and provision of data, and especially to Ms. Niki Koulermou and Mr. Kleopas Hadjicharalambous. The authors would like to acknowledge the ‘EXCELSIOR’ H2020 Teaming project ([www.excelsior2020.eu](http://www.excelsior2020.eu)). This paper is under the auspices of the activities of the ‘ERATOSTHENES: Excellence Research Centre for Earth Surveillance and Space-Based Monitoring of the Environment’—‘EXCELSIOR’ project that has received funding from the European Union’s Horizon 2020 research and innovation programme under Grant Agreement No. 857510 and from the Government of the Republic of Cyprus through the Directorate General for the European Programmes, Coordination, and Development. The authors would also like to acknowledge the CyCLOPS project (<https://cyclops-rpf.eu/>), which stands for Cyprus Continuously Operating Natural Hazards Monitoring and Prevention System (RPF/INFRASTRUCTURES/1216/0050). CyCLOPS is co-financed by the European Union Regional Fund and the Republic of Cyprus through the Research Promotion Foundation. This work is part of the PhD thesis of Marios Tzouvaras that was conducted at the Cyprus University of Technology, Department of Civil Engineering and Geomatics (Eratosthenes Research Group).

**Conflicts of Interest:** The authors declare no conflict of interest.

## References

- Rodrigue, J.P.; Comtois, C.; Slack, B. *The Geography of Transport Systems*, 2nd ed.; Routledge Taylor & Francis: London, UK; New York, NY, USA, 2006. [CrossRef]
- Jenelius, E.; Mattsson, L.G. Road Network Vulnerability Analysis of Area-Covering Disruptions: A Grid-Based Approach with Case Study. *Transp. Res. Part A Policy Pract.* **2012**, *46*, 746–760. [CrossRef]
- Jenelius, E.; Petersen, T.; Mattsson, L.G. Importance and Exposure in Road Network Vulnerability Analysis. *Transp. Res. Part A Policy Pract.* **2006**, *40*, 537–560. [CrossRef]
- Geological Survey Department. *The Seismicity of Cyprus*; Press and Information Office of the Republic of Cyprus: Nicosia, Cyprus, 2012.
- Alexandris, A.; Griva, I.K.; Abarioti, M. Remediation of the Pissouri Landslide in Cyprus. *Int. J. Geoenviron. Case Hist.* **2016**, *4*, 14–28. [CrossRef]
- Geological Survey Department. *Landslides in Cyprus and Their Consequences to Built Environment*; Press and Information Office of the Republic of Cyprus: Nicosia, Cyprus, 2013.
- Geological Survey Department. Geological Survey Department\Ground Suitability. Available online: [http://www.moa.gov.cy/moa/gsd/gsd.nsf/page37\\_en/page37\\_en?OpenDocument](http://www.moa.gov.cy/moa/gsd/gsd.nsf/page37_en/page37_en?OpenDocument) (accessed on 12 January 2020).
- Northmore, K.J.; Charalambous, M.; Hobbs, P.R.N.; Petrides, G. *Engineering Geology of the Kannaviou, 'Melange' and Mamonia Complex Formations—Phiti/Statos Area, S W Cyprus: Engineering Geology of Cohesive Soils Associated with Ophiolites, with Particular Reference to Cyprus*. Report of the EGARP Research Group British Geological Survey, No. EGARP-KW 86/4; Report of the Geological Survey Department of Cyprus, No. G/EG/15. 1986. Available online: <http://nora.nerc.ac.uk/id/eprint/19494/1/WNRR86004.pdf> (accessed on 14 May 2019).
- Northmore, K.J.; Charalambous, M.; Hobbs, P.R.N.; Petrides, G. Complex Landslides in the Kannaviou, Melange, and Mamonia Formations of South-West Cyprus. In *5th International Symposium on Landslides*; Bonnard, C., Ed.; Balkema Publishers: Brookfield, WI, USA, 1988; pp. 263–268.
- Pantazis, T.M. Landslides in Cyprus. *Bulletin* **1969**, *4*, 1–20.
- Charalambous, M.; Petrides, G. Contribution of Engineering Geology in the Planning and Development of Landslide Prone Rural Areas in Cyprus. In *Engineering Geology and the Environment*; Balkema: London, UK, 1997; pp. 1205–1210.
- Hart, A.B.; Ruse, M.E.; Hobbs, P.R.N.; Efthymiou, M.; Hadjicharalambous, K. Assessment of Landslide Susceptibility in Paphos District, Cyprus. In *GRSG-AGM Geoenvironmental Remote Sensing Conference*; The Geological Society of London: London, UK, 2010.
- Hart, A.B.; Hearn, G.J. Landslide Assessment for Land Use Planning and Infrastructure Management in the Paphos District of Cyprus. *Bull. Eng. Geol. Environ.* **2013**, *72*, 173–188. [CrossRef]
- Saha, A.K.; Gupta, R.P.; Arora, M.K. GIS-Based Landslide Hazard Zonation in the Bhagirathi (Ganga) Valley, Himalayas. *Int. J. Remote Sens.* **2002**, *23*, 357–369. [CrossRef]
- Lee, S.; Lee, M.-J. Detecting Landslide Location Using KOMPSAT 1 and Its Application to Landslide-Susceptibility Mapping at the Gangneung Area, Korea. *Adv. Space Res.* **2006**, *38*, 2261–2271. [CrossRef]
- Fourniadis, I.G.; Liu, J.G.; Mason, P.J. Landslide Hazard Assessment in the Three Gorges Area, China, Using ASTER Imagery: Wushan–Badong. *Geomorphology* **2007**, *84*, 126–144. [CrossRef]
- Park, N.-W.; Chi, K.-H. Quantitative Assessment of Landslide Susceptibility Using High-resolution Remote Sensing Data and a Generalized Additive Model. *Int. J. Remote Sens.* **2008**, *29*, 247–264. [CrossRef]
- Pradhan, B. Remote Sensing and GIS-Based Landslide Hazard Analysis and Cross-Validation Using Multivariate Logistic Regression Model on Three Test Areas in Malaysia. *Adv. Space Res.* **2010**, *45*, 1244–1256. [CrossRef]
- Bhattacharya, A.; Arora, M.K.; Sharma, M.L.; Vöge, M.; Bhasin, R. Surface Displacement Estimation Using Space-Borne SAR Interferometry in a Small Portion along Himalayan Frontal Fault. *Opt. Lasers Eng.* **2014**, *53*, 164–178. [CrossRef]
- Mullissa, A.G.; Tolpekin, V.; Stein, A.; Perissin, D. Polarimetric Differential SAR Interferometry in an Arid Natural Environment. *Int. J. Appl. Earth Obs. Geoinf.* **2017**, *59*, 9–18. [CrossRef]
- Da Lio, C.; Tosi, L. Land Subsidence in the Friuli Venezia Giulia Coastal Plain, Italy: 1992–2010 Results from SAR-Based Interferometry. *Sci. Total Environ.* **2018**, *633*, 752–764. [CrossRef] [PubMed]

22. Liosis, N.; Marpu, P.R.; Pavlopoulos, K.; Ouarda, T.B.M.J. Ground Subsidence Monitoring with SAR Interferometry Techniques in the Rural Area of Al Wagan, UAE. *Remote Sens. Environ.* **2018**, *216*, 276–288. [[CrossRef](#)]
23. Tzouvaras, M.; Kouhartsiouk, D.; Agapiou, A.; Danezis, C.; Hadjimitsis, D.G. The Use of Sentinel-1 Synthetic Aperture Radar (SAR) Images and Open-Source Software for Cultural Heritage: An Example from Paphos Area in Cyprus for Mapping Landscape Changes after a 5.6 Magnitude Earthquake. *Remote Sens.* **2019**, *11*, 1766. [[CrossRef](#)]
24. Morishita, Y.; Lazecky, M.; Wright, T.J.; Weiss, J.R.; Elliott, J.R.; Hooper, A. LiCSBAS: An Open-Source InSAR Time Series Analysis Package Integrated with the LiCSAR Automated Sentinel-1 InSAR Processor. *Remote Sens.* **2020**, *12*, 424. [[CrossRef](#)]
25. Di Martire, D.; Tessitore, S.; Brancato, D.; Ciminelli, M.G.; Costabile, S.; Costantini, M.; Graziano, G.V.; Minati, F.; Ramondini, M.; Calcaterra, D. Landslide Detection Integrated System (LaDIS) Based on in-Situ and Satellite SAR Interferometry Measurements. *Catena* **2016**, *137*, 406–421. [[CrossRef](#)]
26. Bovenga, F.; Pasquariello, G.; Pellicani, R.; Refice, A.; Spilotro, G. Landslide Monitoring for Risk Mitigation by Using Corner Reflector and Satellite SAR Interferometry: The Large Landslide of Carlantino (Italy). *Catena* **2017**, *151*, 49–62. [[CrossRef](#)]
27. Strozzi, T.; Klimeš, J.; Frey, H.; Caduff, R.; Huggel, C.; Wegmüller, U.; Rapre, A.C. Satellite SAR Interferometry for the Improved Assessment of the State of Activity of Landslides: A Case Study from the Cordilleras of Peru. *Remote Sens. Environ.* **2018**, *217*, 111–125. [[CrossRef](#)]
28. Pieraccini, M.; Mecatti, D.; Noferini, L.; Luzi, G.; Franchioni, G.; Atzeni, C. SAR Interferometry for Detecting the Effects of Earthquakes on Buildings. *NDT E Int.* **2002**, *35*, 615–625. [[CrossRef](#)]
29. Lin-lin, G.; Cheng, E.; Polonska, D.; Rizos, C.; Collins, C.; Smith, C. Earthquake Monitoring in Australia Using Satellite Radar Interferometry. *Wuhan Univ. J. Nat. Sci.* **2003**, *8*, 649–658. [[CrossRef](#)]
30. Dong, Y.; Li, Q.; Dou, A.; Wang, X. Extracting Damages Caused by the 2008 Ms 8.0 Wenchuan Earthquake from SAR Remote Sensing Data. *J. Asian Earth Sci.* **2011**, *40*, 907–914. [[CrossRef](#)]
31. Pritchard, M.E.; Simons, M. A Satellite Geodetic Survey of Large-Scale Deformation of Volcanic Centres in the Central Andes. *Nature* **2002**, *418*, 167–171. [[CrossRef](#)] [[PubMed](#)]
32. Pavez, A.; Remy, D.; Bonvalot, S.; Diament, M.; Gabalda, G.; Froger, J.-L.; Julien, P.; Legrand, D.; Moisset, D. Insight into Ground Deformations at Lascar Volcano (Chile) from SAR Interferometry, Photogrammetry and GPS Data: Implications on Volcano Dynamics and Future Space Monitoring. *Remote Sens. Environ.* **2006**, *100*, 307–320. [[CrossRef](#)]
33. Meyer, F.J.; McAlpin, D.B.; Gong, W.; Ajadi, O.A.; Arko, S.; Webley, P.W.; Dehn, J. Integrating SAR and Derived Products into Operational Volcano Monitoring and Decision Support Systems. *ISPRS J. Photogramm. Remote Sens.* **2015**, *100*, 106–117. [[CrossRef](#)]
34. Schaefer, L.N.; Di Traglia, F.; Chaussard, E.; Lu, Z.; Nolesini, T.; Casagli, N. Monitoring Volcano Slope Instability with Synthetic Aperture Radar: A Review and New Data from Pacaya (Guatemala) and Stromboli (Italy) Volcanoes. *Earth Sci. Rev.* **2019**, *192*, 236–257. [[CrossRef](#)]
35. Bitelli, G.; Bonsignore, F.; Carbognin, L.; Ferretti, A.; Strozzi, T.; Teatini, P.; Tosi, L.; Vittuari, L. Radar Interferometry-Based Mapping of the Present Land Subsidence along the Low-Lying Northern Adriatic Coast of Italy. In Proceedings of the EISOLS 2010, Queretaro, Mexico, 17–22 October 2010; pp. 279–286.
36. Hsieh, C.S.; Shih, T.Y.; Hu, J.C.; Tung, H.; Huang, M.H.; Angelier, J. Using Differential SAR Interferometry to Map Land Subsidence: A Case Study in the Pingtung Plain of SW Taiwan. *Nat. Hazards* **2011**, *58*, 1311–1332. [[CrossRef](#)]
37. D’Aranno, P.; Di Benedetto, A.; Fiani, M.; Marsella, M. Remote sensing technologies for linear infrastructure monitoring. *ISPRS Int. Arch. Photogramm. Remote Sens. Spat. Inf. Sci.* **2019**, *XLII-2/W11*, 461–468. [[CrossRef](#)]
38. Closson, D.; Milisavljevic, N. InSAR Coherence and Intensity Changes Detection. In *Mine Action—The Research Experience of the Royal Military Academy of Belgium*; InTech: London, UK, 2017; p. 23. [[CrossRef](#)]
39. Rocca, F.; Prati, C.; Guarnieri, A.M.; Ferretti, A. Sar Interferometry and Its Applications. *Surv. Geophys.* **2000**, *21*, 159–176. [[CrossRef](#)]
40. Rosen, P.A.; Hensley, S.; Joughin, I.R.; Li, F.K.; Madsen, S.N.; Rodriguez, E.; Goldstein, R.M. Synthetic Aperture Radar Interferometry. *Proc. IEEE* **2000**, *88*, 333–382. [[CrossRef](#)]
41. Zebker, H.A.; Villasenor, J. Decorrelation in Interferometric Radar Echoes. *IEEE Trans. Geosci. Remote Sens.* **1992**, *30*, 950–959. [[CrossRef](#)]

42. Burrows, K.; Walters, R.J.; Milledge, D.; Spaans, K.; Densmore, A.L. A New Method for Large-Scale Landslide Classification from Satellite Radar. *Remote Sens.* **2019**, *11*, 237. [[CrossRef](#)]
43. Lu, C.-H.; Ni, C.-F.; Chang, C.-P.; Yen, J.-Y.; Chuang, R. Coherence Difference Analysis of Sentinel-1 SAR Interferogram to Identify Earthquake-Induced Disasters in Urban Areas. *Remote Sens.* **2018**, *10*, 1318. [[CrossRef](#)]
44. Abdelfattah, R.; Nicolas, J.M. Interferometric Synthetic Aperture Radar Coherence Histogram Analysis for Land Cover Classification. In Proceedings of the 2006 2nd International Conference on Information & Communication Technologies, Damascus, Syria, 24–28 April 2006; Volume 1, pp. 343–348. [[CrossRef](#)]
45. Parihar, N.; Das, A.; Rathore, V.S.; Nathawat, M.S.; Mohan, S. Analysis of L-Band SAR Backscatter and Coherence for Delineation of Land-Use/Land-Cover. *Int. J. Remote Sens.* **2014**, *35*, 6781–6798. [[CrossRef](#)]
46. Khalil, R.Z. InSAR Coherence-Based Land Cover Classification of Okara, Pakistan. *Egypt. J. Remote Sens. Space Sci.* **2018**, *21*, S23–S28. [[CrossRef](#)]
47. Pan, Z.; Hu, Y.; Wang, G. Detection of Short-Term Urban Land Use Changes by Combining SAR Time Series Images and Spectral Angle Mapping. *Front. Earth Sci.* **2019**, *13*, 495–509. [[CrossRef](#)]
48. Yun, H.W.; Kim, J.R.; Choi, Y.S.; Lin, S.Y. Analyses of Time Series InSAR Signatures for Land Cover Classification: Case Studies over Dense Forestry Areas with L-Band SAR Images. *Sensors* **2019**, *19*, 2830. [[CrossRef](#)]
49. Erten, E.; Lopez-Sanchez, J.M.; Yuzugullu, O.; Hajnsek, I. Retrieval of Agricultural Crop Height from Space: A Comparison of SAR Techniques. *Remote Sens. Environ.* **2016**, *187*, 130–144. [[CrossRef](#)]
50. Tamm, T.; Zalite, K.; Voormansik, K.; Talgre, L. Relating Sentinel-1 Interferometric Coherence to Mowing Events on Grasslands. *Remote Sens.* **2016**, *8*, 802. [[CrossRef](#)]
51. Liu, C.; Chen, Z.; Shao, Y.; Chen, J.; Hasi, T.; Pan, H. Research Advances of SAR Remote Sensing for Agriculture Applications: A Review. *J. Integr. Agric.* **2019**, *18*, 506–525. [[CrossRef](#)]
52. Suga, Y.; Takeuchi, S. Application of JERS-1 InSAR for Monitoring Deforestation of Tropical Rain Forest. *Int. Geosci. Remote Sens. Symp.* **2000**, *1*, 432–434. [[CrossRef](#)]
53. Canisius, F.; Brisco, B.; Murnaghan, K.; Van Der Kooij, M.; Keizer, E. SAR Backscatter and InSAR Coherence for Monitoring Wetland Extent, Flood Pulse and Vegetation: A Study of the Amazon Lowland. *Remote Sens.* **2019**, *11*, 720. [[CrossRef](#)]
54. Durieux, A.M.; Calef, M.T.; Arko, S.; Chartrand, R.; Kontgis, C.; Keisler, R.; Warren, M.S. Monitoring Forest Disturbance Using Change Detection on Synthetic Aperture Radar Imagery. In *Applications of Machine Learning*; Zelinski, M.E., Taha, T.M., Howe, J., Awwal, A.A., Iftkharuddin, K.M., Eds.; SPIE: San Diego, CA, USA, 2019; p. 39. [[CrossRef](#)]
55. Ban, Y.; Zhang, P.; Nascetti, A.; Bevington, A.R.; Wulder, M.A. Near Real-Time Wildfire Progression Monitoring with Sentinel-1 SAR Time Series and Deep Learning. *Sci. Rep.* **2020**, *10*, 1322. [[CrossRef](#)] [[PubMed](#)]
56. Hirschmugl, M.; Deutscher, J.; Sobe, C.; Bouvet, A.; Mermoz, S.; Schardt, M. Use of SAR and Optical Time Series for Tropical Forest Disturbance Mapping. *Remote Sens.* **2020**, *12*, 727. [[CrossRef](#)]
57. Monti-Guarnieri, A.V.; Brovelli, M.A.; Manzoni, M.; Mariotti d’Alessandro, M.; Molinari, M.E.; Oxoli, D. Coherent Change Detection for Multipass SAR. *IEEE Trans. Geosci. Remote Sens.* **2018**, *56*, 6811–6822. [[CrossRef](#)]
58. Uemoto, J.; Moriyama, T.; Nadai, A.; Kojima, S.; Umehara, T. Landslide Detection Based on Height and Amplitude Differences Using Pre- and Post-Event Airborne X-Band SAR Data. *Nat. Hazards* **2019**, *95*, 485–503. [[CrossRef](#)]
59. Jung, J.; Yun, S.-H. Evaluation of Coherent and Incoherent Landslide Detection Methods Based on Synthetic Aperture Radar for Rapid Response: A Case Study for the 2018 Hokkaido Landslides. *Remote Sens.* **2020**, *12*, 265. [[CrossRef](#)]
60. Bouaraba, A.; Acheroy, M.; Closson, D. Coherent Change Detection Performance Using High-Resolution SAR Images. *Int. J. Eng. Res. Technol.* **2013**, *2*, 3160–3166.
61. Bouaraba, A.; Milisavljević, N.; Acheroy, M.; Closson, D. Change Detection and Classification Using High Resolution SAR Interferometry. In *Land Applications of Radar Remote Sensing*; InTech: London, UK, 2014. [[CrossRef](#)]
62. Veci, L. *Sentinel-1 Toolbox—TOPS Interferometry Tutorial*; European Space Agency; Array Systems Computing Inc.: Toronto, ON, Canada, 2016.



63. Braun, A.; Veci, L. *Sentinel-1 Toolbox—TOPS Interferometry Tutorial*; European Space Agency; SkyWatch Space Applications Inc.: Waterloo, ON, Canada, 2020.
64. Plank, S.; Twele, A.; Martinis, S. Landslide Mapping in Vegetated Areas Using Change Detection Based on Optical and Polarimetric SAR Data. *Remote Sens.* **2016**, *8*, 307. [[CrossRef](#)]
65. Watanabe, M.; Thapa, R.B.; Ohsumi, T.; Fujiwara, H.; Yonezawa, C.; Tomii, N.; Suzuki, S. Detection of Damaged Urban Areas Using Interferometric SAR Coherence Change with PALSAR-2. *Earth Planets Space* **2016**, *68*, 131. [[CrossRef](#)]
66. Cyprus Tourism Organisation. Petra Tou Romiou (The Rock of the Greek). Nicosia, Cyprus; pp. 1–7. Available online: [https://www.visitcyprus.com/files/audio\\_guides/written\\_form/Petra\\_tou\\_Romiou\\_afigisi\\_en.pdf](https://www.visitcyprus.com/files/audio_guides/written_form/Petra_tou_Romiou_afigisi_en.pdf) (accessed on 14 May 2019).
67. Stow, D.A.V.; Braakenburg, N.E.; Xenophontos, C. The Pissouri Basin Fan-Delta Complex, Southwestern Cyprus. *Sediment. Geol.* **1995**, *98*, 245–262. [[CrossRef](#)]
68. ESA. Open Access Hub. Available online: <https://scihub.copernicus.eu/> (accessed on 28 June 2019).
69. ESA. SNAP|STEP. Available online: <https://step.esa.int/main/toolboxes/snap/> (accessed on 17 July 2019).
70. Sentinel Hub. NDVI (Normalized Difference Vegetation Index)|Sentinel Hub. Available online: <https://www.sentinel-hub.com/eoproducts/ndvi-normalized-difference-vegetation-index> (accessed on 9 March 2020).
71. Beguería, S. Validation and Evaluation of Predictive Models in Hazard Assessment and Risk Management. *Nat. Hazards* **2006**, *37*, 315–329. [[CrossRef](#)]
72. Eng, J. ROC Analysis: Web-Based Calculator for ROC Curves. Available online: <http://www.rad.jhmi.edu/jeng/javarad/roc/JROCFITi.html> (accessed on 18 March 2020).



© 2020 by the authors. Licensee MDPI, Basel, Switzerland. This article is an open access article distributed under the terms and conditions of the Creative Commons Attribution (CC BY) license (<http://creativecommons.org/licenses/by/4.0/>).